THE UNIVERSITY OF CHICAGO

FORCE EXERTION AND TRANSMISSION IN CROSS-LINKED ACTIN NETWORKS

A DISSERTATION SUBMITTED TO

THE FACULTY OF THE DIVISION OF THE PHYSICAL SCIENCES

AND

THE FACULTY OF THE DIVISION OF THE BIOLOGICAL SCIENCES

AND THE PRITZKER SCHOOL OF MEDICINE

IN CANDIDACY FOR THE DEGREE OF

DOCTOR OF PHILOSOPHY

GRADUATE PROGRAM IN BIOPHYSICAL SCIENCES

BY

SAMANTHA STAM

CHICAGO, ILLINOIS

AUGUST 2017

Table of Contents

LIST OF FIGURES ..... **vi**

LIST OF TABLES ..... **ix**

ACKNOWLEDGEMENTS ..... **x**

ABSTRACT ..... **xii**

CHAPTER 1 INTRODUCTION **1**

1.1 BASIC ACTOMYOSIN INTERACTIONS: AN UNDERSTANDING DEVELOPED FROM MUSCLE FIBER CONTRACTION 1

1.2 CONTRACTING MUSCLES AND OTHER ACTOMYOSIN SYSTEMS ARE TYPES OF ACTIVE MATTER 3

Active matter: definition and examples 3

Active materials can contain contractile or extensile force dipoles 4

1.3 CYTOSKELETAL NETWORK FEATURES THAT AFFECT CONTRACTILITY AND OTHER PHYSICAL PROPERTIES OF INTERNAL FORCE GENERATION AND TRANSMISSION 5

Myosin II isoform properties that may affect magnitude, duration, and mechanosensitivity of intracellular forces 5

Physical properties of biopolymers and their networks affect contractility and spatial propagation of internal forces 8

Properties of motors and biopolymers that are examined in this thesis 10

1.4 SUMMARY 11

1.5 PUBLICATIONS 11

CHAPTER 2 ISOFORMS CONFER CHARACTERISTIC FORCE GENERATION AND MECHANOSENSATION BY MYOSIN II FILAMENTS 12

2.1 INTRODUCTION 12

2.2 METHODS 13

Model Description 13

Simulations 16

Benchmarking tests: A simple two-state model captures variation in motor performance for myosin II isoforms 20

2.3 RESULTS 23

The number of myosin heads, the motor duty ratio, and external force determine myosin filament processivity 23

Motor properties and external stiffness shape the magnitude and stability of force generation 26

Determinants of characteristic time scale of force buildup 29

Force-dependent myosin kinetics produced a switch-like transition from non-processive to processive force generation 30

Mechanical cues regulate the switch to processive force generation 32

Myosin II isoform performance in elastic networks 34

2.4 DISCUSSION 39

CHAPTER 3 FILAMENT RIGIDITY AND CONNECTIVITY TUNE THE DEFORMATION MODES OF ACTIVE BIOPOLYMER NETWORKS 42

3.1 INTRODUCTION 42

3.2 METHODS 44

Protein purification 44
Microscopy sample preparation 44
Fluorescence microscopy 46
Image Analysis 46
Simulation methods 47
3.3 RESULTS 48
Networks of cross-linked rigid bundles are contractile with a short correlation length 48
Rigidity controls the anisotropy of contractile deformations 54
Uniaxial contraction arises from actomyosin sliding arrested by cross-linker accumulation 59
Motors drive aster formation within rigid bundles without cross-links via uniaxial, extensile forces 64
3.4 DISCUSSION 67
CHAPTER 4 CONCLUSIONS 70
REFERENCES 74

List of Figures

Figure 1.1 Sarcomeric muscle contraction..... 2

Figure 1.2 Potential deformation modes in biopolymer-motor systems..... 5

Figure 2.1 A two state cross-bridge model reproduced expected gliding velocity and force-velocity curve of motor clusters..... 15

Figure 2.2 Dependence of effective duty ratio (ρ_d) on the spacing of myosin motors and actin filament binding sites in simulated gliding assays..... 17

Figure 2.3 Rapid approach to steady state from an initially unbound condition during simulated unloaded gliding..... 19

Figure 2.4 Effective internal resistance of elastic crossbridge limits gliding velocities..... 21

Figure 2.5 Scaling of unloaded gliding velocity vs. motor density and force vs. velocity curves 23

Figure 2.6 Myosin filament processivity depends on motor properties and external force..... 24

Figure 2.7 Dependence of motor cluster processivity on unloaded duty ratio $\rho_d(0)$ and external load F_{ext} 25

Figure 2.8 Myosin filament size and actin stiffness determined the magnitude and stability of force generation 27

Figure 2.9 Dependence of force buildup on unloaded duty ratio ρd(0) and environmental stiffness K. 28

Figure 2.10 The characteristic time required for processive motors to build to stall, t_{build}, scaled as $F_{max}V_{max}^{-1}K^{-1}$ 30

Figure 2.11 Force-dependent myosin kinetics produced a switch-like transition into processive state 31

Figure 2.12 A small constant force superimposed on a linear load can trigger processive force generation 33

Figure 2.13 Myosin isoforms are predicted to display varying types of behavior on elastic substrates due to differences in t_{attach} and t_{build} 36

Figure 2.14 Coassembly of non-muscle myosin IIA and IIB 37

Figure 3.1 Networks of rigid bundles are contractile with a short correlation length 49

Figure 3.2 Fascin bundles contain ~ 8 actin filaments 51

Figure 3.3 Networks form polarity-sorted asters with varying structure 53

Figure 3.4 Deformations are highly biaxial and uniaxial in networks of semi-flexible filaments and rigid bundles respectively 55

Figure 3.5 Networks have different contributions of biaxial and uniaxial deformations at varying length scales 56

Figure 3.6 $P_{biaxial}$ at varying length scales has different trends over time for different networks. 57

Figure 3.7 Activation of biaxial or uniaxial deformations in semi-flexible filament and rigid bundle networks respectively coincides with correlated motion and contractility 58

Figure 3.8 Simulations indicate cross-link dependent contractility over a wide range of filament stiffness 60

Figure 3.9 Uniaxial contractility is caused by arrested filament sliding 62

Figure 3.10 Myosin re-organizes rigid bundles lacking filamin cross-links via extensile uniaxial forces 64

Figure 3.11 Data for network of rigid bundles without cross-links. Unscaled L_{corr} as a function of time. 65

Figure 3.12 Minimum of $<\nabla \cdot v_{act}>$ for PIV vectors calculated with varying time delay and length scale 66

Figure 3.13 State space on force generation in active matter comprised of motors and filaments 68

List of Tables

Figure 2.1 Simulation parameter values 16

Figure 2.2 Tunable parameter values used to represent myosin isoforms in Fig. 2.1 19

Acknowledgements

I owe a great deal of gratitude to many people who have supported me both scientifically and personally over the years spent preparing this dissertation. First, I thank my advisor, Margaret Gardel. Her lab environment has allowed me to pursue a unique kind of science using ideas from both biology and physics. Ed Munro also acted as an unofficial second advisor to me. I particularly thank him for his patient teaching style while training an experimentalist to do simulations.

I benefited from the participating in the Physics Department/MRSEC REU program during which I worked in the Gardel lab for one summer as an undergrad. Todd Thoresen, a postdoc in the lab at the time, mentored me throughout the summer. He had good advice on topics ranging from actin and myosin biochemistry to surviving in Chicago--all of which I probably needed help with. The REU management, namely Sid Nagel's lab, Eileen Sheu, and Brenda Thomas, also created a supportive and friendly environment that helped me decide to come back for graduate school.

I also thank the faculty and staff associated with my graduate program in Biophysical Sciences. Adam Hammond had the task of training/reigning in the first-year biophysicists during our initial "boot camp" lab course. Michele Wittels and Julie Feder have always made themselves available when I needed help with various issues from academic to administrative. They have certainly made my life as a graduate student run more smoothly.

My interactions with other students and postdocs have led to valuable contributions to this thesis. The project written about in Chapter 3 was a team effort led initially by Kim Weirich, Shiladitya Banerjee, and I. We spent many seemingly fruitless hours of discussion in the GCIS atrium at first, but the project eventually took off. Without ideas and advice from Kim and Shila,

the experiments and analysis of Chapter 3 would respectively be just skeletons of what they currently are. Simon Freedman also later entered the project and used simulations to give us important insights about the experiments. In Chapter 2, Jon Alberts contributed much of the original simulation package and ideas behind the motor benchmarking tests. Various current and former members of Dave Kovar's lab including Dennis Zimmermann, Alyssa Harker, Cristian Suarez, and Yujie Li offered instruction on protein purification and handling.

Finally, I have depended on the support of friends and family to help me through graduate school. I thank my undergrad roommate and friend Alison Umbarger. She and I have debated the advantages and disadvantages of science vs. engineering as a career path so much that it certainly has helped me make a more informed decision about my future. Kim Weirich and Anne Juggernauth are also friends of mine who have offered support and career advice. I could write an entire dissertation about the support of my family, but it would likely violate the formal requirements of this thesis and would also embarrass them. My brother Dan and I started graduate school around the same time, and he was someone I could talk to about the inevitable struggles those early years entailed. My parents, Duane and Louanne Stam, have always been there to offer words of encouragement when I needed them the most. Thanks to them, I have learned to remain humble enough to question my own judgement and seek advice from other people, but also to sometimes trust my own instincts. Their inquisitiveness about topics ranging from plants to weather patterns to human social structure instilled, in me, a desire to understand and document how the world works. Thank you all for the love and support that allowed me to develop into the thing that finished this dissertation.

Abstract

Cells are responsive to external cues in their environment telling them to proliferate or migrate within their surrounding tissue. Sensing of cues that are mechanical in nature, such stiffness of a tissue or forces transmitted from other cells, is believed to involve the cytoskeleton of a cell. The cytoskeleton is a complex network of proteins consisting of polymers that provide structural support, motor proteins that remodel these structures, and many others. We do not yet have a complete understanding of how cytoskeletal components respond to either internal or external mechanical force and stiffness. Such an understanding should involve mechanisms by which constituent molecules, such as motor proteins, are responsive to mechanics. Additionally, physical models of how forces are transmitted through biopolymer networks are necessary.

My research has focused on networks formed by the cytoskeletal filament actin and the molecular motor protein myosin II. Actin filaments form networks and bundles that form a structural framework of the cell, and myosin II slides actin filaments. In this thesis, we show that stiffness of an elastic load that opposes myosin-generated actin sliding has a very sharp effect on the myosin force output in simulations. Secondly, we show that the stiffness and connectivity of cytoskeletal filaments regulates the contractility and anisotropy of network deformations that transmit force on material length scales. Together, these results have implications for predicting and interpreting the deformations and forces in biopolymeric active materials.

Chapter 1 Introduction

1.1 Basic actomyosin interactions: an understanding developed from muscle fiber contraction

The cytoskeleton is a complex assortment of proteins that provides structure for a cell and is important for any dynamic process involving cellular shape change or transport of material within a cell. These include cell motion, proliferation, and growth amongst others. Importantly, such processes are likely regulated by both the biochemical as well as mechanical properties of the protein constituents. The relative importance of these properties, and the amount of detail necessary in producing models that explain or predict cellular behaviors under different conditions, are large outstanding questions in cell biology.

The interactions between actin and myosin II are associated with a number of specific processes that fall under the general functions mentioned above. A few examples include actin-myosin II arrays during muscle contraction (1), constriction of actin rings during cytokinesis (2), and pulsed contraction of actomyosin foci that drive cytoplasmic transport (3). These processes could potentially be controlled by dozens of proteins that regulate polymerization and depolymerization of actin and myosin (e. g. formin and cofilin), connectivity of actin filament networks (e. g. alpha-actinin and filamin), local actin filament orientation (e.g. fascin and Arp 2/3), and the affinity of other proteins that bind actin (e.g. tropomyosin) (4, 5).

However, the example of muscle contraction shows that developing an understanding of basic actin-myosin interactions can provide a great deal of insight into a complex process. As was

shown in landmark experiments in the 1930s (6), contraction of intact muscle fibers proceeds at a certain speed that depends on the external resisting force exerted on the fiber. The relationship between the contraction speed and the resisting force is hyperbolic (Fig. 1.1a). Over the following decades before the 1980s, theoretical modeling and structural evidence from x-ray, electron microscopy, and phase contrast microscopy (Fig. 1.1b) indicated that relative sliding of actin driven by myosin could be sufficient to drive muscle contraction with this basic force-velocity relationship (7-12). This model is described below. The ability of myosin to cause actin sliding (13, 14) and the sufficiency of actin and myosin to reproduce the force-velocity curve of muscle

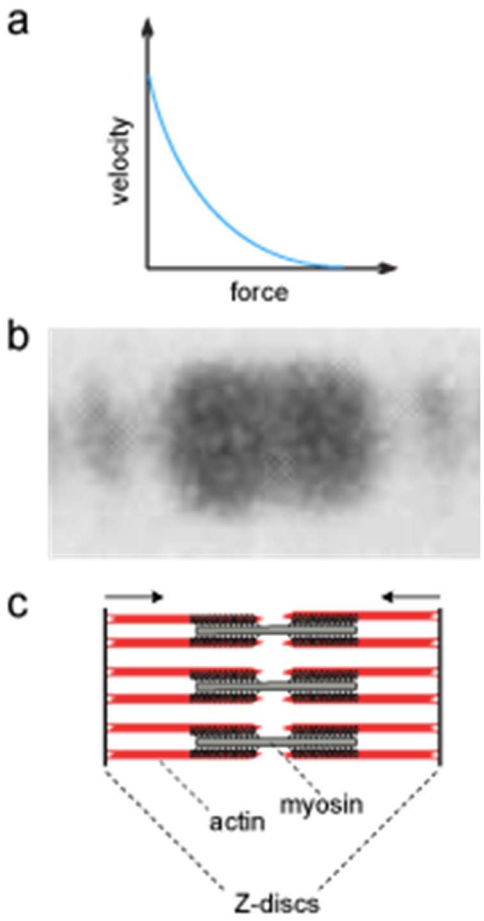

Figure 1.1 Sarcomeric muscle contraction. (a) Muscle contraction proceeds with a velocity that depends hyperbolically on the opposing force. (b) Phase contrast image of a muscle sarcomere from ref. 10. (c) Cartoon representation of structures in (b).

(15, 16) would later be directly observed experimentally as imaging and micromanipulation technologies evolved.

The basic structure of actin-myosin arrays in a muscle sarcomere is depicted in Fig. 1.1c. Myosin filaments, which are composed of several hundred motor domains in skeletal muscle (17) are at the center of actin filaments. The actin filaments are polar, meaning that myosin only walks toward the "barbed" ends of the actin. The barbed ends are outward from the location of the myosin and are attached to Z-discs via compliant connections. This geometry enforces that the sarcomere contracts rather than extends, because the myosin draws barbed ends toward itself.

1.2 Contracting muscles and other actomyosin systems are types of active matter

Active matter: definition and examples

The biological systems described above are examples of biological active matter**.** Active materials are defined by the presence of internal building blocks that exert forces and produce motion at the microscale (18). Early studies of active matter were theoretical examinations of flocking behavior of self-motile organisms or particles on substrates (19, 20). Experimental systems including motile colloids, bacterial suspensions, and networks of purified cytoskeletal motors and filaments (18). These materials present unique challenges compared to traditional passive materials, where a well-defined external force may be applied to a material to measure its deformation properties. A general goal of these studies is to develop fundamental physical models of force production and motion within these materials that are analogous to the one of muscle contraction descried in the previous section. More specifically, developing physical models

requires information about the direction, magnitude, and duration of the internally applied forces, as well as the propagation of those forces through the material.

Active materials can contain contractile or extensile force dipoles

Simple models of force application within active materials have been constructed from their basic physics. At low Reynold's number, the net force exerted by an adherent cell or a myosin filament on its surroundings is expected to be vanishingly small given the lack of large accelerations in these systems. The sum of the forces exerted via direct physical interaction between the active force-generating element (e.g., cell or myosin filament) and the substrate it binds to will balance those of viscous drag from its motion. For small objects such as a myosin filament that moves at speeds ~ 1 μm/s, the drag forces are typically small (< 0.05 pN) compared to the forces it applies to actin filaments (> 5 pN) (21). The simplest internally applied force in an active material that follows these general patterns and conserves momentum is a force dipole exerting opposing forces of nearly equal magnitude on its substrate (22). This force dipole model is relevant in so-called "wet" active materials, as opposed to "dry" active materials, where the active agents push against a substrate and theoretical models do not enforce momentum conservation (18-20).

The active materials described above can produce contractile or extensile force dipoles. Myosin and actin filaments within muscle sarcomeres form contractile force dipoles due to the geometry of the polar actin filaments already described (Fig. 1.1c). In systems with disordered filament polarity, they also can form extensile force dipoles depending on the degree of filament overlap. When the motor is near the filament pointed ends, the configuration is contractile like muscles (Fig. 1.2a), and as they reach the barbed end, the deformation propagates extensile forces

(Fig. 1.2b). Adherent mammalian cells typically produce contractile forces (22). Depending on the arrangement of their flagella, bacterial cells can be either "pullers" or "pushers" and thus respectively exert contractile or extensile forces (23). Through a combination of *in vitro* experiments and agent-based simulations, my work has involved developing a better understanding of how basic properties of biopolymer filaments and motors regulate force exertion and propagation. Below is a summary of previous knowledge of how properties that are specific to cytoskeletal polymers and motors may regulate intracellular forces.

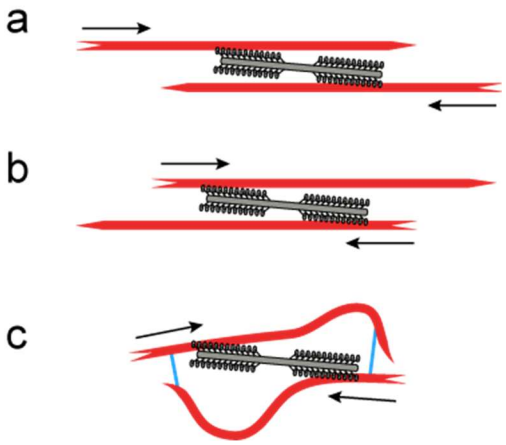

Figure 1.2 Potential deformation modes in biopolymer-motor systems (a) Contractile configuration where myosin is near the actin pointed ends. (b) Extensile configuration where myosin is near the actin barbed ends. (c) Contractile configuration occuring due to actin filament buckling

1.3 Cytoskeletal network features that affect contractility and other physical properties of internal force generation and transmission

Myosin II isoform properties that may affect magnitude, duration, and mechanosensitivity of intracellular forces

All myosin II isoforms polymerize into filaments with multiple myosin motor head domains. Each one of these motor heads hydrolize ATP as a part of a cycle of attachment to actin, a

powerstroke or step-like motion of the actin filament, and detachment from the actin. The biochemical rate constants for transitions between different steps of this cycle, as well as the number of motor heads in a filament, are variable for different isoforms of myosin II in muscle and nonmuscle cells. As a result, the duty ratio, or the fraction of time that an individual motor head is bound to actin, and the actin gliding speed are two key properties that vary for the different isoforms. The effects that isoform-specific characteristics may have on force production are described below.

The duration of local myosin-generated forces is affected by two of these properties: the duty ratio of individual myosin motors, and the number of myosin motors contained in one filament. With the possible exception of the myosin IIB isoform (24, 25) individual myosin II dimers are low duty-ratio or non-processive, meaning that they do not take more than one step along actin filaments before dissociating (26-28). However, a myosin filament has a higher effective duty ratio because its multiple motors are able to maintain association with actin. This may allow force buildup to occur over a period of multiple seconds before stochastic unbinding of the entire filament causes relaxation of the force (29, 30). Experiments using *in vitro* purified proteins (30) or cells (31, 32) have shown evidence of elastic force buildup and recoil. However, other *in vivo* actomyosin networks undergo directional flow on longer time scales (3, 33), indicating that force duration is variable in different physiological contexts. The density of myosin filaments, their content of isoforms with different duty ratios, and the size of the filaments could affect these behaviors. In muscle cells, the duty myosin duty ratios are ~1-5% (28), while the

nonmuscle isoforms may range from 5% to 60% (24-27). The number of motors in filaments ranges from several hundred in muscle cells (17, 34, 35) to 10-50 in nonmuscle cells (36, 37).

The magnitude of local forces is also regulated by motor kinetics and myosin filament size. Individual myosin II motor domains stall at a force magnitude of ~1-5 pN (25, 38, 39), but their duty ratio and number will determine the maximum force possible for a myosin II filament. Furthermore, force buildup in cells must compete with various phenomena that cause relaxation of force such as unbinding of actin cross-linking proteins or depolymerization of actin filaments, which occur on timescales of 1-100 s (40-42). Myosin II isoforms have unloaded actin-gliding speeds ranging from 50 nm/s to 7 μm/s (43-45), and it is possible that their force buildup rate limits their total force output in some dynamic networks.

A final feature that is shared by myosin II isoforms is that the unbinding rate of a motor depends on the force it is under—a property that allows motor activity to be regulated by environmental forces or stiffness. Myosin II forms a type of bond with actin known as a catch-bond, in which unbinding of a motor is inhibited by forces that oppose the powerstroke (46-48). This force-dependence was predicted by theoretical modeling (49) before its direct measurement with single-molecule studies, and is sufficient to produce the force velocity curve of muscle depicted in Fig. 1.1a, which would be linear in the absence of force dependence (49). The effect of the myosin catch-bond in non-sarcomeric contexts is less understood. A few previous studies

have assumed the myosin catch-bond to be responsible for the ability of non-muscle cells to adjust their force output depending on the mechanical stiffness of their environment (50-52).

Physical properties of biopolymers and their networks affect contractility and spatial propagation of internal forces

Key physical properties of biopolymer networks include the spatial arrangement of the biopolymer filaments, the filament connectivity, and filament stiffness. As detailed below, these features may regulate the local deformations in these networks. As a result, the forces transmitted on varying length scales will depend on these properties.

Contractility is the most extensively studied feature of network deformations. Actomyosin structures in cells other than skeletal muscle may contract even in the absence of sarcomeric structure (5). Contraction is also very robust in disordered networks of purified actin, myosin, and typically an actin cross-linking protein (53-56), indicating that simple properties of these few components are sufficient to produce contractility. As was described in Fig. 1.2a and 1.2b, both contractility and extensility of actin filament sliding could potentially occur depending on the relative position of the filaments, so the reasons for this dominance of contractility in random networks are not obvious. In other *in vitro* reconstitutions of purified microtubules and the motor protein kinesin, the proteins form extensile bundles (57-60). Many properties of the experimental systems in these references differ, and the causes of contractility versus extensility are not understood.

One mechanism of regulating contractility could involve controlling the degree of overlap between biopolymer filaments depicted in Fig. 1.2 Simple models have suggested that net contractility of sliding could occur, for example, if motors slow down or stall near the biopolymer

filament barbed or plus ends (61, 62). This could inhibit the extensile phase of sliding depicted in Fig. 1.2b, or could introduce contractile relative sliding of parallel actin filaments (62).

Models of the microtubule/kinesin systems mentioned above have indicated that net extensility will naturally occur if binding affinity and filament sliding rate is uniform along the filament (59, 60). This may be understood as follows. If a motor is initially bound near the pointed ends of two filaments in the contractile configuration of Fig. 1.2a and proceeds to slide the two filaments until reaching the completely extended configuration of Fig. 1.2b, then the entire process is neither contractile nor extensile. However, motors do not necessarily always bind in configurations near the filament pointed ends. Therefore, extensility will dominate the relative sliding of antiparallel filaments. Extensility is further enhanced because the configuration with maximal overlap of two antiparallel filaments has more sites for motors to become bound to both filaments, thereby increasing the magnitude of the pushing force (59, 60).

Alternatively, asymmetry in the deformation of individual actin polymers, rather than their relative motion, could lead to differences in contractility. The stiffness associated with stretching an actin filament beyond its fully extended length is ~ 44 pN/nm (63). On the other hand, the critical compressive force required to buckle an actin filament may be estimated by the Euler buckling equation:

$$F = \frac{\pi^2 EI}{L^2}$$

where E is the Young's modulus, I is the second moment of area, and L is the filament length. The value of this threshold force is < 1 pN for actin filaments with lengths greater than 1 μm (64). Actin buckling could dissipate compressive forces to yield an overall contractile transmitted force dipole (Fig. 1.2c). Actin buckling has been predicted to be a cause of contraction in disordered networks by theoretical studies (65, 66). Furthermore, comparison of theory to experiments (67)

or direct experimental observation of filament deformations (55, 68) has indicated that buckling is indeed important for contractile deformation in some actin networks. This suggests that mechanical stiffness of individual filaments will influence contractility. Other network properties that influence the length scale of buckling or the ability to build or relax force relative to the threshold buckling force will be important. Recent modeling (66, 67) and experiments (67) have indicated that optimal buckling-based contraction will occur at intermediate densities of actin cross-linkers and motors.

Finally, contractility could be produced in disordered biopolymer networks due to regulation of the relative angles of actin filaments. In this mechanism, myosin motors "zipper" pairs actin filaments that are initially at high angles to one another to make them more aligned (69). Recent theory indicates that this mechanism may dominate in small regions of parameter space where myosin density and filament cross-link density are varied (70).

Properties of motors and biopolymers that are examined in this thesis

Here, I have focused on a subset of the properties mentioned above. In simulations, I vary the properties of myosin II filaments and focus on (1) the properties that are known to vary amongst myosin II isoforms (number of motors per filament, motor duty ratio, and motor speed) and (2) the force-dependent catch bond that all myosin II isoforms share. The first of these is important because much is known about how large groups of myosin II motors operate in skeletal muscle, and much is known about varying myosin II isoforms at the single molecule level, but the behavior of intermediate-size ensembles typical of nonmuscle cells is not as well-characterized. The second is examined because previous models seeking to understand how cells respond to environmental

stiffness have included assumptions of myosin's sensitivity to force and stiffness (50-52) without informing their assumptions with detailed simulations of catch-bond dynamics.

In experiments, I focus on varying the biopolymer stiffness and connectivity. Increasing the stiffness is important because it should suppress the buckling instability that recent studies have suggested is critical for actomyosin contraction (55, 65-68). Secondly, understanding the effects of changing the network connectivity builds on previous work observing that the length scale of network contractions is affected by actin cross-linking proteins (53, 54, 71) without characterizing how this is caused by varying deformation modes including filament buckling. We hypothesize that increasing the network connectivity will bias the deformations toward buildup of stress and buckling rather than filament sliding, thereby increasing contractility.

1.4 Summary

In this thesis, I employ computational and experimental approaches to study the physical properties of materials constructed from actin filaments and myosin II. This involves both studies of the local exertion of force by myosin motors through simulation and studies of force transmission on longer length scales through in vitro experiments and image analysis. A primary focus is to understand how the properties of force dipoles in active biopolymer networks are affected by mechanical properties of actin networks.

1.5 Publications

The material in Chapter 2 has been previously published in (72) and the material in Chapter 3 has been submitted for publication (73).

Chapter 2 Isoforms confer characteristic force generation and mechanosensation by myosin II filaments

2.1 Introduction

Actomyosin contractility involves interactions of myosin II motors with actin filament (F-actin) arrays and powers a wide range of physiological processes including muscle contraction (74, 75), cell migration (76, 77), cell division (78, 79) and tissue morphogenesis (80, 81). These diverse contractile functions are mediated by functionally distinct myosin II isoforms operating within actin arrays that range from highly ordered muscle sarcomeres to highly disordered networks. Contractile forces generated by myosin II are sensitive to mechanical context. This mechanosensitivity has been best studied in muscle, but may also allow non-muscle cells to sense and respond to mechanical signals such as external force or stiffness (50, 82, 83). However, we still lack a quantitative understanding of how myosin force generation depends on the interplay of motor properties and cellular mechanics.

The swinging cross-bridge model for myosin II has played a key role in connecting the molecular properties of single motors to the macroscopic dynamics of contractile force production (84). The cross-bridge model has been used mainly in the context of skeletal muscle contraction where the large number of motors and sarcomeric organization make it possible to relate microscopic dynamics to tissue scale response in a straightforward way (7, 49, 85-90). More recently, cross-bridge models have been used to study the dynamics of force production and filament translocation in non-sarcomeric contexts (91-94). However, these models have yet to be

used in a more systematic analysis of how force production varies with isoform-specific motor properties, filament size, and substrate (i.e. F-actin network) compliance.

Here, we used computer simulations based on a simple form of the swinging cross-bridge model to explore how motor properties and environmental stiffness shape the magnitude, stability, and mechanosensitivity of force generation by myosin II filaments. We found that force generation was regulated by competing timescales associated with force build up via motor activity and actomyosin attachment. Using parameters consistent with different myosin II isoforms, we identify three characteristic regimes. First, skeletal muscle myosin filaments can produce large forces with relatively small build up times over a large range of stiffness values. Second, filaments of non-muscle myosin IIB serve as stable cross-linkers, but are poor force generators due to their exceedingly slow cross-bridge cycle. Finally, filaments of non-muscle myosin IIA behave as low affinity cross-linkers at low forces or stiffness, but can undergo switch-like transitions to a productive force-generating state with small changes in motor parameters or mechanical context. The basis for these switch-like transitions is positive feedback between force buildup and attachment mediated by force-dependent detachment (catch bond behavior) of individual myosin motors. Our results clarify how isoform variations in microscopic motor properties and the local mechanical environment can lead to regulation of cellular contractility by myosin II motors.

2.2 Methods

Model Description

The main goal of this study was to characterize how force production by myosin II filaments depends on the interplay of network compliance and basic motor properties. To this end, we used

a simple version of the cross-bridge model that captured the essential phenomenology of motor/filament interactions with a minimal number of parameters. These parameters could be tuned to capture variations in motor properties, filament size and network compliance. Below we describe the design and implementation of this model and a set of benchmarking tests that validate its use for the purposes of our analysis.

We started with the basic mechanochemical cycle shared by all myosin II motors (Fig. 2.1a), in which: (i) hydrolysis of ATP places the ATP-bound motor (Myo.ATP) into a "primed" (Myo.ADP.Pi) state that binds weakly to F-actin; (ii) Pi release, transition to a strongly bound state, and an internal conformation change (the "powerstroke") converts the stored energy of ATP hydrolysis into force applied to the actin filament; (iii) ADP release followed by (iv) ATP rebinding and filament unbinding complete the cycle. We simplified as follows: First, we assumed that the weak-strong binding transition (step ii) could be represented by a first order rate constant with no force dependence as in (91). This ignored the possibility that the free energy cost of the powerstroke transition could become limiting under external loads (49, 92-94). Second, we assumed the weak-strong transition is rate limiting relative to ATP hydrolysis (26, 27) and combined Myo.ATP and Myo.ADP.Pi into a single unbound state, which neglected the small reverse rate of ATP hydrolysis. Third, consistent with *in vitro* studies, we assumed that ATP is sufficiently abundant that force-dependent ADP release is rate limiting for motor detachment (26, 27, 95, 96). With these assumptions, the mechanochemical cycle simplifies to a two-state cross-bridge model with a first order binding rate constant $k_{on.}$ and a force-dependent detachment rate k_{off} (Fig. 2.1a).

We represented the cross-bridge as an elastic element tethered at position X_0 to a rigid substratum representing the backbone of the myosin filament or the surface of a glass coverslip

(Fig. 2.1b). We assumed that the cross-bridge bound actin in a pre-strained (post-powerstroke) state at $X = X_0 + d_{step}$ and exerted a force $F(X) = k_{x\text{-}bridge}(X\text{-}X_0)$ before unbinding.

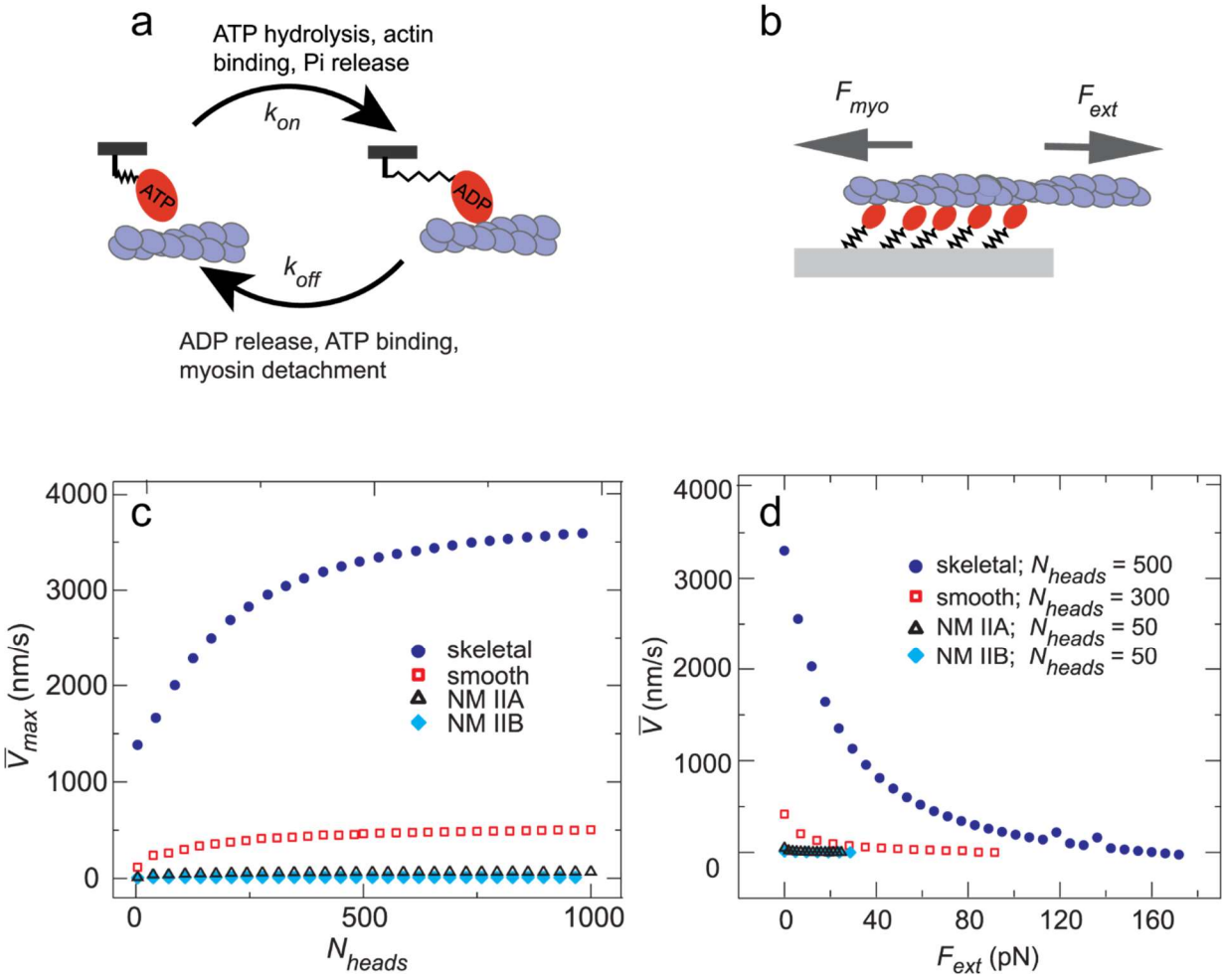

Figure 2.1 A two state cross-bridge model reproduced expected gliding velocity and force-velocity curve of motor clusters. (a) Description of mechanochemical cycle: myosins strongly attached actin filaments at a rate k_{on} and detached with rate k_{off}. (b) Simulation setup: motor heads were attached to a fixed surface. The heads pulled with a force F_{myo} against an external force F_{ext}. (c) The mean gliding velocity of an unloaded actin filament (V_{max}) as a function of N_{heads} for parameters consistent with different myosin isoforms, described in Table 1. Only the velocity while at least one myosin head was attached was considered. (d) Mean gliding velocity with varying F_{ext}. Each data point is the average of 10^7 samples over 100 s of simulation time. The standard error of the velocity was less than the size of the data points.

All myosin II isoforms studied thus far exhibit "catch-bond" behavior in which forces that oppose the motor (resisting loads) reduce the rate of motor detachment from F-actin, while

assisting loads increase motor detachment (46-48). Above a critical force the bond behaves like a traditional slip bond (47). To represent this behavior, we used the force-dependent form of k_{off} determined experimentally for skeletal muscle myosin II in (47):

$$k_{off}(F) = k_{off}(0)\left[\alpha_{catch} exp\left(-{}^{Fx_{catch}}/_{k_BT}\right) + \alpha_{slip} exp\left({}^{Fx_{slip}}/_{k_BT}\right)\right] \quad (1)$$

where the force F is positive for a resisting load, k_B is Boltzmann's constant, T is temperature, x_{catch} and x_{slip} are characteristic bond lengths, and α_{catch} and α_{slip} are prefactors controlling the weights of the catch and slip components (Table 1). The unloaded detachment rate $k_{off}(0)$ can be tuned to model variation in detachment rates and duty ratios across different isoforms (see below).

Table 2.1 Parameter Values

Name	Description	Value	Reference
N_{heads}	number of heads	variable; 2-1000	see Table 2
k_{on}	binding rate	variable; 0.2-10 s^{-1}	see Table 2
$k_{off}(0)$	unloaded unbinding rate	variable; 0.35-500 s^{-1}	see Table 2
α_{catch}	See Eqn (1)	0.92	(47)
α_{slip}	See Eqn (1)	0.08	(47)
x_{catch}	See Eqn (1)	2.5 nm	(47)
x_{slip}	See Eqn (1)	0.4 nm	(47)
$k_{off}(F)$	force dependent unbinding rate	See Eqn (1)	(47)
d_{step}	step size	5.5 nm	(46)
$K_{x\text{-}bridge}$	cross-bridge stiffness	0.7 pN/nm	(46)

Simulations

We considered a linear ensemble of myosin crossbridges, attached at 5 nm intervals to a rigid substrate (Fig. 2.1b) that bound and exerted force upon an actin filament. The actin filament was subjected to a constant external load (Fig. 2.1b) and/or attached to a linear spring that represented

stiffness of the surrounding network (Fig. 2.8a). Binding sites for myosin II were arrayed at 2.7 nm intervals and motors bound only to the closest site. The spacing of motors and binding sites we used differed from experimentally measured values (28, 97). However, we verified that these differences had modest effects on the outcomes of our simulations and that these effects were negligible given the main goals of this work, which were to study the effects of varying motor properties and network stiffness on force production (see Fig. 2.2).

Figure 2.2 Dependence of effective duty ratio (ρ_d)on the spacing of myosin motors and actin

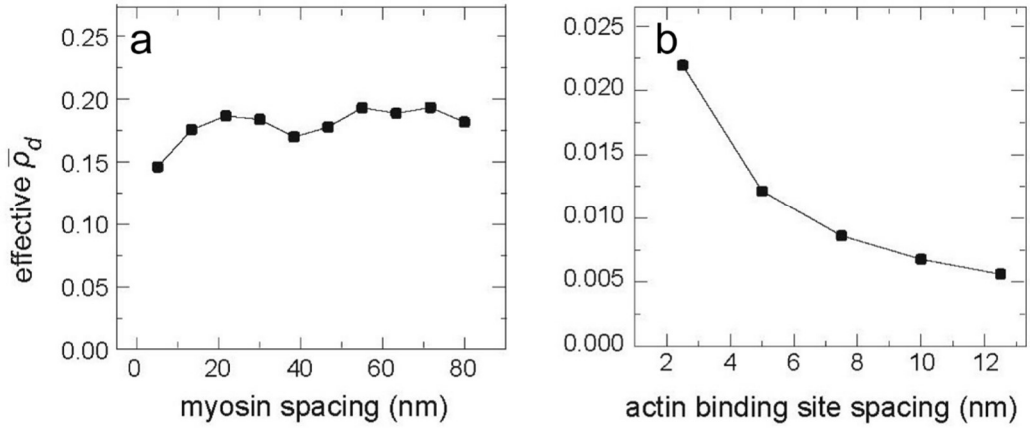

filament binding sites in simulated gliding assays. (a) Dependence of ρ_d on motor spacing using parameters for non-muscle myosin IIB from Table 2 and N_{heads} = 50. The spacing that we used in our simulations was 5 nm, which is smaller than the experimentally estimated value of 40 nm reported in reference 28. However, varying this value from 5 to 80 had little effect on the average duty ratio even for these relatively high duty ratio motors. (b) Dependence of ρ_d on the spacing of filament binding sites for motors approximating skeletal muscle myosin II with N_{heads} = 50. The spacing that we used, 2.7 nm, differed from the experimentally measured value of 5.5 nm reported in reference 96. However, higher values lead to a reduction in average duty ratio due to binding-site limited attachment of motors even for the relatively low-duty ratio skeletal muscle parameters. The value that we used yields an appropriate duty ratio. Each data point is the average of 1000 values over a 100 s simulation.

We sampled binding and unbinding rates stochastically to determine transitions between bound and unbound states (98). Between transitions, we computed the instantaneous F-actin velocity by numerically solving the following equation of motion for the F-actin:

$$0 = -\gamma\dot{x} - F_{myo} + F_{ext} \quad (2)$$

where F_{myo} is the total force exerted by the myosin crossbridges, F_{ext} is the external force on the filament, and γ is a drag coefficient of $4\text{x}10^{-4}$ pN·s/nm. This method is inefficient relative to approaches that assume instantaneous mechanical relaxation between binding/unbinding events (91-93). We chose to use it here because it extends naturally to simulations of larger motor/filament ensembles and because computational time was not rate-limiting for our analysis.

Simulations began with all motors in an unbound state. However, the distribution of filament velocities converged rapidly relative to the timescale of typical simulations (Fig. 2.3), and thus the results we report are independent of initial conditions. For most results, we report mean values obtained by averaging over the duration of at least one simulation (see figure legends for details). For a given quantity X, we use $\bar{X}$ to denote the mean value and σ to represent its standard deviation.

In a few cases (data in Fig. 2.13 and Fig. 2.14), we indicate values obtained by curve fitting using Wolfram *Mathematica* with the superscript *fit*.

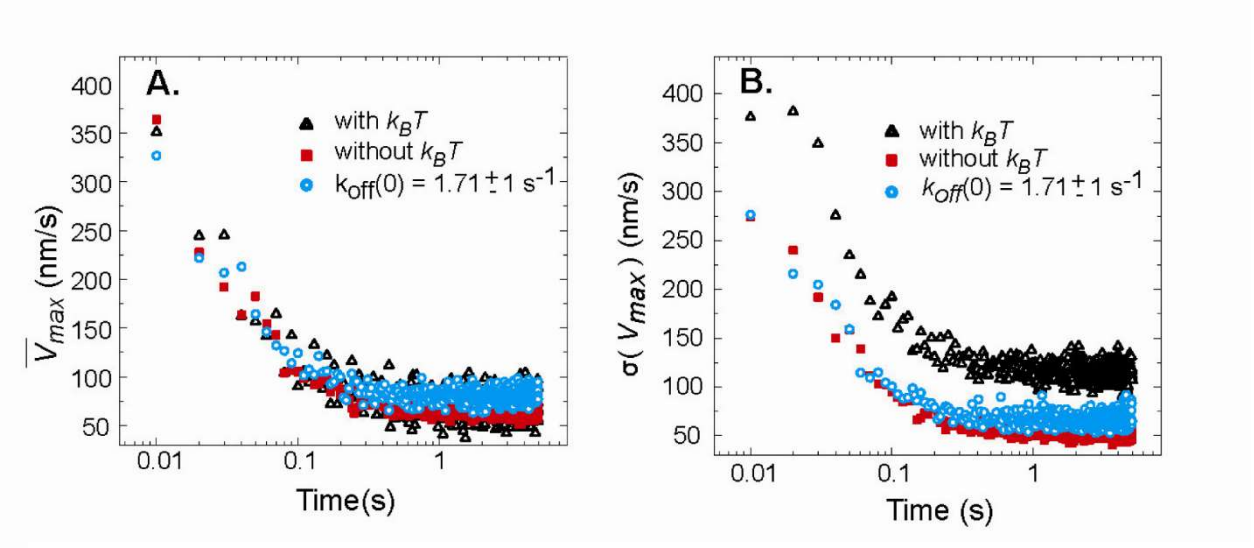

Figure 2.3 Rapid approach to steady state from an initially unbound condition during simulated unloaded gliding. (a) Average timecourse of unloaded gliding velocity with or without thermal noise or random variation in the value of $k_{off}(0)$ across the ensemble. (b) Standard deviations corresponding to the averages in (a). Each data point is the average or standard deviation from 100 individual simulations. Parameter choices: NM IIA parameters from Table 2 and N_{heads} = 500.

Table 2.2 Tunable parameter values used to represent myosin isoforms in Fig. 2.1

Parameter	Isoform	Value	Reference
$k_{off}(0)$	skeletal	500 s^{-1}	(99)
	smooth	22 s^{-1}	(95, 96)
	nonmuscle IIA	1.71 s^{-1}	(27)
	nonmuscle IIB	0.35 s^{-1}	(26)
k_{on}	skeletal	10 s^{-1}	(100)
	smooth	1 s^{-1}	(95)
	nonmuscle IIA	0.2 s^{-1}	(27)
	nonmuscle IIB	0.2 s^{-1}	(26)
N_{heads}	skeletal	500	(101)
	smooth	300	(34, 35)
	nonmuscle IIA	50	(36)
	nonmuscle IIB	50	(36)

Benchmarking tests: A simple two-state model captures variation in motor performance for myosin II isoforms

We first tested the ability of the model to capture variation in myosin II isoform performance as measured in gliding assays and force-velocity curves. We assigned isoform-specific values for the attachment rate k_{on} and the unloaded detachment rate $k_{off}(0)$ based on *in vitro* studies (see Table 2). For each set of parameters, we measured the average unloaded gliding velocity, $\bar{V}_{max}$, as a function of the number of myosin heads (N_{heads}). In all four cases, $\bar{V}_{max}$ increased monotonically with N_{heads} and saturated at high values (Fig. 2.1c). The maximal gliding velocities agreed reasonably well with those observed experimentally for these four isoforms (28, 102, 103). The saturation of $\bar{V}_{max}$ with increasing N_{heads} was consistent with experimental gliding filament assays (28, 104) and previous models (91, 92, 104) and reflected the transition to a "detachment-limited" regime in which newly attached motors face increasing opposition from previously attached cross-bridges that become negatively strained before detachment (Fig. 2.4). Notably, the isoform-specific curves collapsed when we scaled the velocity by the maximum (saturated) value, and the x-axis by the unloaded duty ratio $\rho_d(0) = k_{on}/(k_{on} + k_{off}(0))$ (Fig. 2.5a).

We further verifed that our simulations reproduced the concave force-velocity relationship observed experimentally (6, 16) and in previous models (7, 49, 85-90) (Fig. 2.1d). Again, we found that isoform-specific data collapsed onto a single curve when the force and velocity were

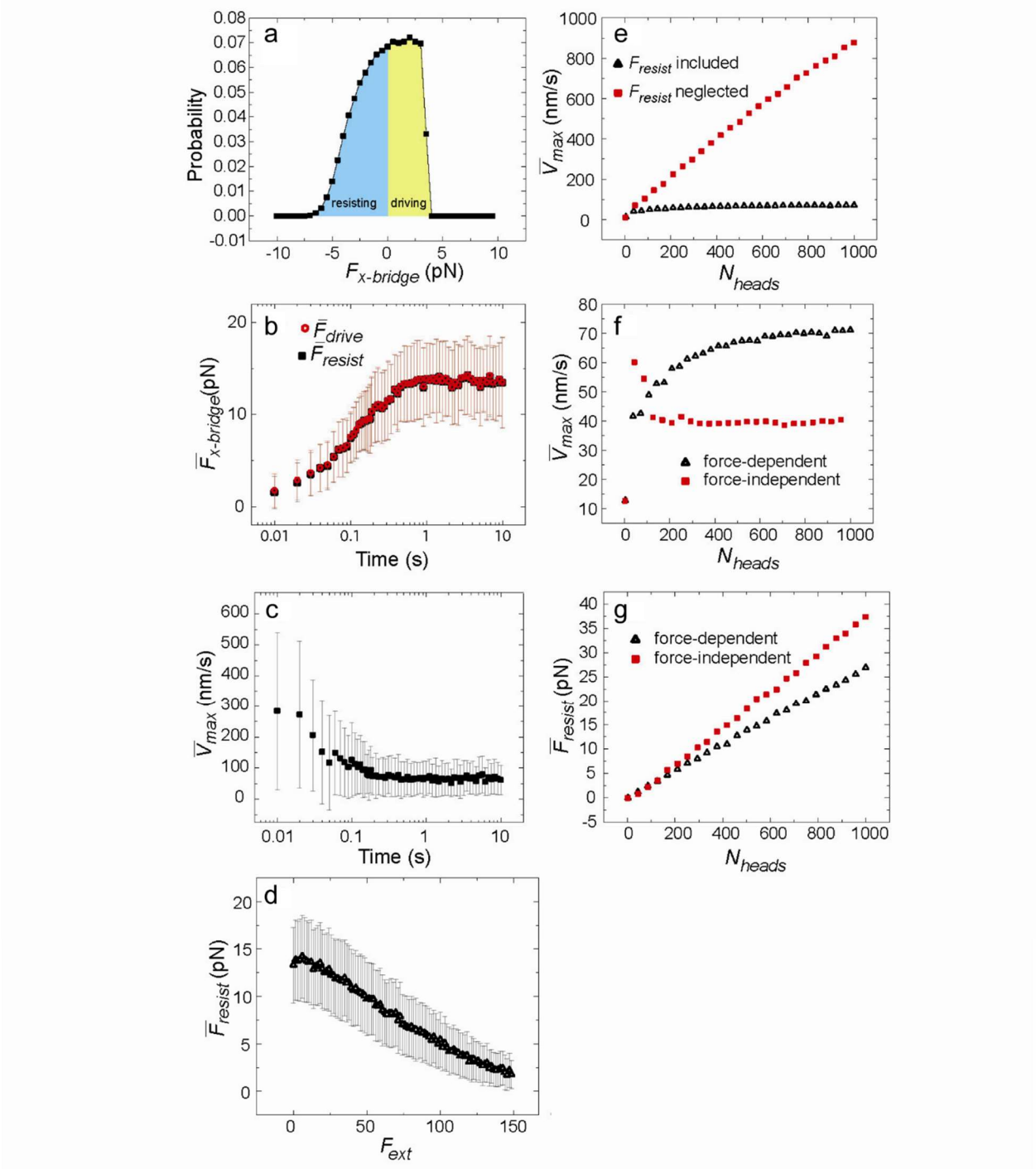

Figure 2.4 Effective internal resistance of elastic crossbridge limits gliding velocities. (a) Distribution of positive (driving) and negative (resisting) forces on individual myosin cross-bridges during steady state gliding of an unloaded actin filament. (b) Accumulation of driving and resisting forces from an initial state in which all motors are unbound. (c) Evolution of the unloaded gliding velocity, V_{max}, from the same initial condition as in (b).

Figure 2.4, continued (d) The resisting force from negatively strained crossbridges decreases with F_{ext}. (e) Comparison of average unloaded gliding velocities in simulations where resisting forces from negatively strained crossbridges are either included or neglected in the equation of motion. (f) Comparison of average unloaded gliding velocities with force-dependent or independent k_{off}. (g) The resisting force from negatively strained crossbridges decreases with use of force-dependent kinetics. Panels (a) and (d)-(g) display data from 1000 samples averaged over 100 s of simulation time. Panels (b) and (c) display average data over 100 independent runs. Error bars indicate standard deviaion. Parameter choices: (a-g) NM IIA parameters from Table 2, (a-d) $N_{heads} = 500$.

scaled by $\bar{V}_{max}$ and the average ensemble stall force $\bar{F}_{max}$, respectively (Fig. 2.5b). In all cases, the average ensemble stall force $\bar{F}_{max}$ matched the expected value given by:

$$\bar{F}_{max} = F_{sm} N_{heads} \rho_d(F_{sm}) \tag{3}$$

where $F_{sm} = K_{x\text{-}bridge,}\, d_{step}$ is the stall force for a single motor, and $\rho_d\,(F_{sm}) = k_{on}[k_{on}+k_{off}(F_{sm})]^{-1}$ is the duty ratio of a single motor at stall.

These data confirm that our simple two-state model captures the expected qualitative dependence of velocity on force and gliding speed on motor density. By varying just two parameters (k_{on}, and k_{off}), we can approximate the observed variation in unloaded duty ratios and gliding speeds for different myosin II isoforms. Additional mechanochemical steps would be required to explain more detailed behavior such as oscillations or pauses observed in actin gliding (49, 94) or effects of limiting ATP binding (91) or hydrolysis rates. Isoform-specific differences in other parameters (e.g. x_{catch} (46, 47)) will also affect motor performance. This variation would affect the data collapse seen in Fig. 2.5a and Fig. 2.5b. Nevertheless, this simple model is adequate

to assess how variation in binding rates and the presence of load-dependent release impact force buildup in different mechanical contexts.

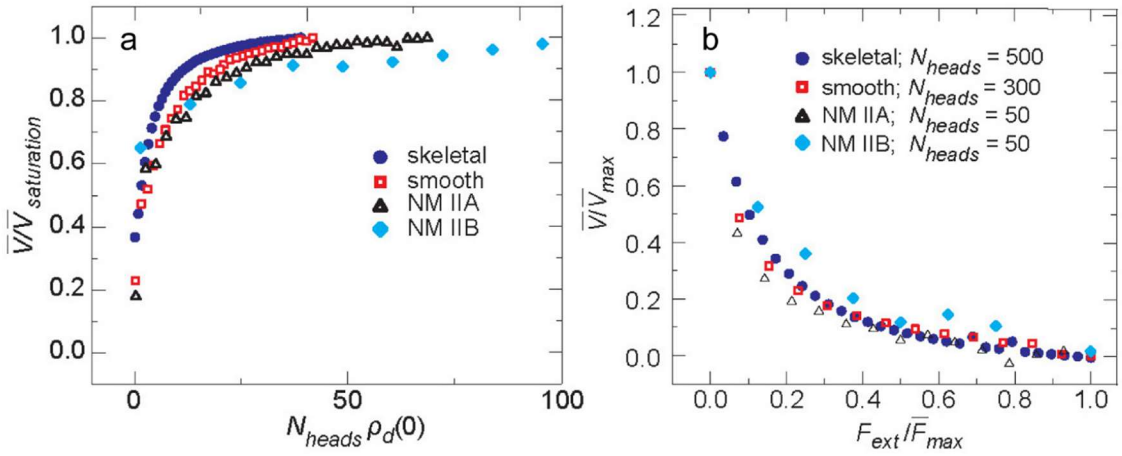

Figure 2.5 Scaling of unloaded gliding velocity vs. motor density and force vs. velocity curves. (a) Isoform-specific plots of gliding velocity vs. motor density from Fig. 2.1c collapse when the horizontal axis is scaled by plateau velocity at large N_{heads} and the vertical axis is scaled by the unloaded motor duty ratio. (b) Isoform-specific plots of force vs. velocity from Fig. 2.1d collapse when the horizontal and vertical axes are scaled respectively by $\bar{F}_{max}$ and $\bar{V}_{max}$. Each data point is the average of 10^7 samples over 100 s of simulation time.

2.3 Results

The number of myosin heads, the motor duty ratio, and external force determine myosin filament processivity

We began by assessing the dependence of motor filament processivity on motor properties. Because individual myosin II motors are non-processive (26-28), assembly of multiple motors into filaments is essential for stable engagement. Consistent with this, increasing either N_{heads} or $\rho_d(0)$ drove a transition from cycles of rapid attachment/detachment to stable, processive translocation

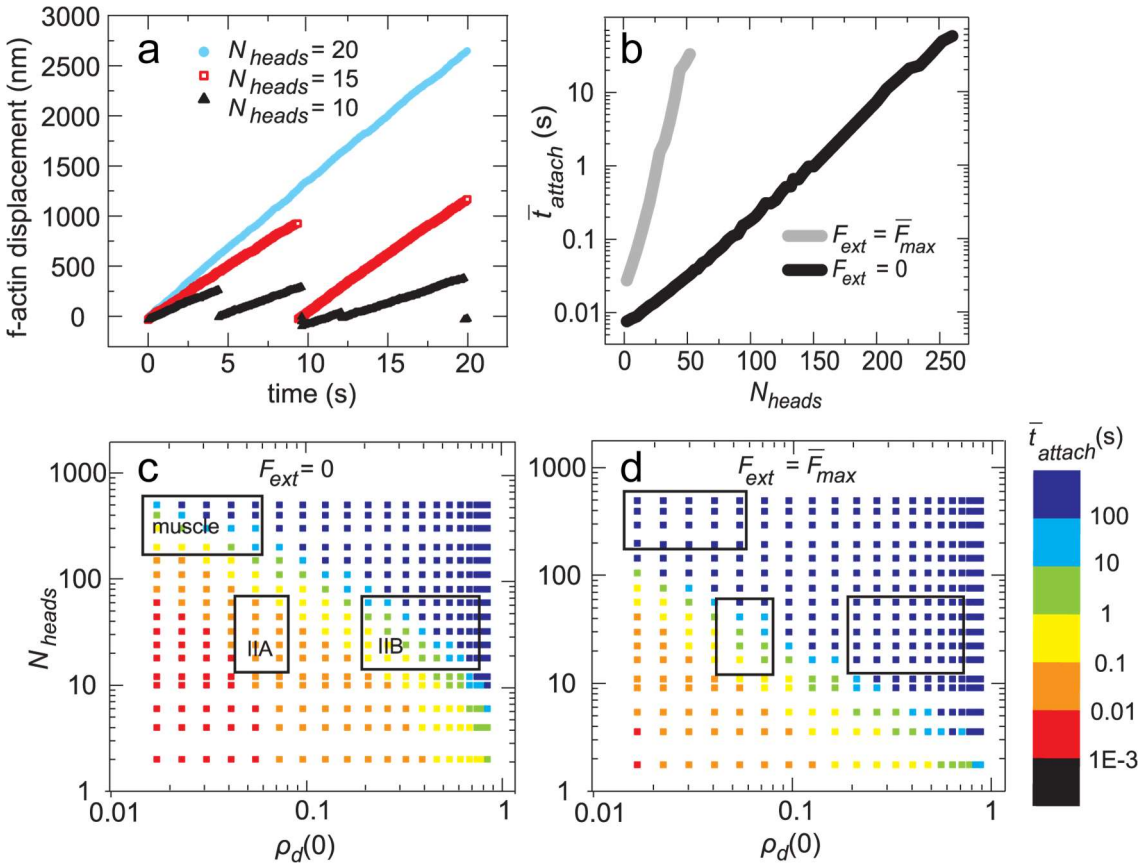

Figure 2.6 Myosin filament processivity depends on motor properties and external force. (a) Simulated F-actin trajectories for different values of N_{heads}. The actin filament was assumed to return to its original position upon release by the myosin. Each curve represents a single simulation. (b) The mean attached time as a function of N_{heads} showed a shift under stalled compared to unloaded conditions. (c) Mean attached time on an unloaded F-actin for a range of N_{heads} and $\rho_d(0)$. The boxes indicate literature values for muscle myosins, non-muscle myosin IIB, and non-muscle myosin IIA (see main text for references) starting at the top left and going clockwise. (d) Increased mean attached time for a stalled F-actin over same range as in (c). Parameter values in (a): $\rho_d(0) = 0.05$ ($k_{on} = 10$ s^{-1}, $k_{off}(0) = 191$ s^{-1}), $F_{ext} = 4$ pN, (b): $\rho_d(0) = 0.05$ ($k_{on} = 10$ s^{-1} and $k_{off}(0) = 191$ s^{-1}), (c) and (d) $k_{on} = 10$ s^{-1}. Averages in (b), (c), and (d) were taken over 1000 s of simulation time. The standard error in (b) was smaller than the data points.

(Fig. 2.6a and Fig. 2.7a). Consistent with a previous model (40), the mean attached time ($\bar{t}_{attach}$) increased exponentially with both N_{heads} (Fig. 2.6b, black curve) and $\rho_d(0)$ (Fig. 2.7c, black curve).

Strikingly, the dependence of attachment time on N_{heads} and $\rho_d(0)$ was sharply affected by the presence of an external load. As expected from the force-dependent release kinetics of myosin II (46-48), increasing an external load from 0 to 10 pN for fixed values of N_{heads} and $\rho_d(0)$ both

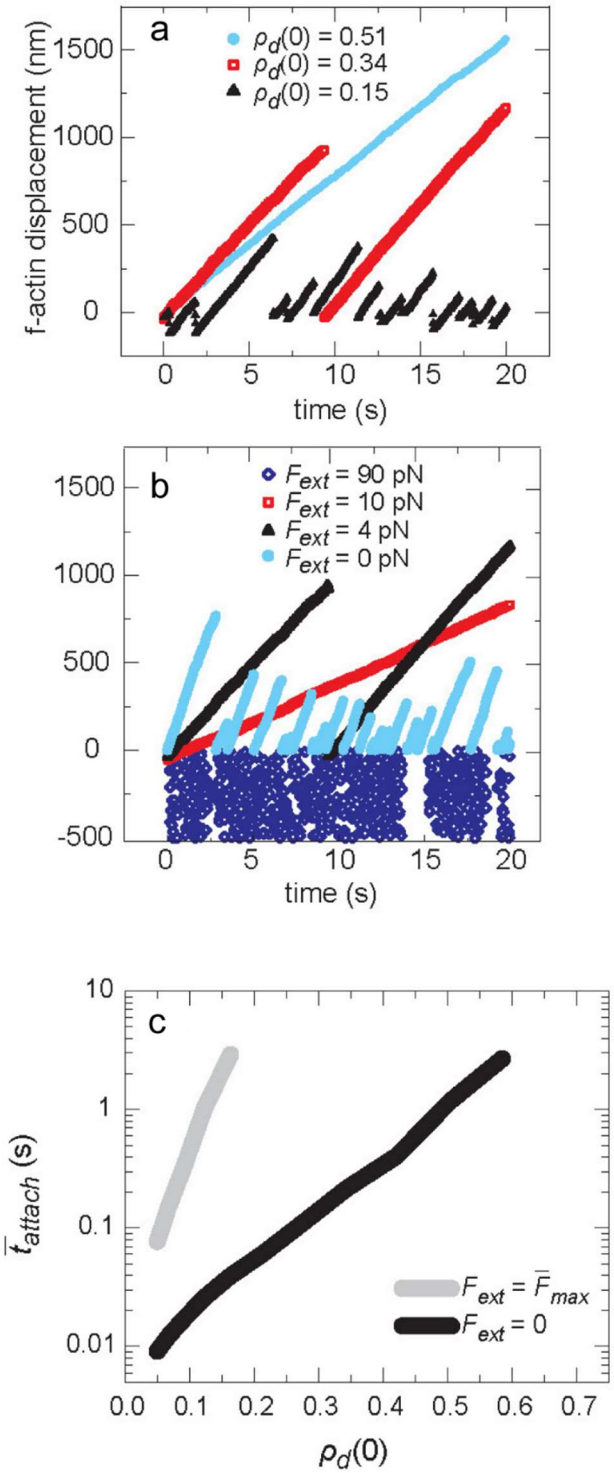

Figure 2.7 Dependence of motor cluster processivity on unloaded duty ratio $\rho_d(0)$ and external load F_{ext}. (a) and (b) Simulated actin filament trajectories for different values of $\rho_d(0)$ (a) or F_{ext} (b). (c) Dependence of mean attachment time ($\bar{t}_{attac}$) on duty ratio $\rho_d(0)$ is exponential and significantly sharper for stalled vs. unloaded conditions. Parameter values in (a-c): k_{on} = 10 s^{-1}, N_{heads} = 15, (a): F_{ext} = 4 pN, and (b): $\rho_d(0)$ = 0.34 ($k_{off}(0)$ = 19 s^{-1}). In (c), averages were taken over 100 s of simulation time.

dominated at forces greater than the stall force of the myosin cluster resulting in negative F-actin displacements (Fig. 2.7b, diamonds). In addition, the exponential rise in $\bar{t}_{attach}$ with N_{heads} (Fig. 2.6b) or $\rho_d(0)$ (Fig 2.7c) was significantly steeper for filaments subjected to a stall force (F_{ext} = $\bar{F}_{max}$ given by equation (3)) than for unloaded filaments. Thus, external loads steepen the response of $\bar{t}_{attach}$ to motor properties.

To quantify the potential magnitude of this effect for different myosin II isoforms, we constructed phase plots of $\bar{t}_{attach}$ vs. filament size and duty ratio for unloaded (Fig. 2.6c) and stalled (Fig. 2.6d) filaments. We then identified regions in these phase plots corresponding to experimentally measured ranges of filament size and motor duty ratio for skeletal or smooth muscle (28, 34, 35, 101), non-muscle IIA (27, 36, 37) and non-muscle IIB isoforms (24, 26, 36, 37). Comparing each matched regions across Figs. 2.6c and 2.6d suggests that attachment times could vary up to several orders of magnitude between the unloaded and stalled conditions. Thus, changes in myosin filament processivity due to forces from the surrounding environment could be significant for myosin II filaments *in vivo*.

Motor properties and external stiffness shape the magnitude and stability of force generation

We then examined how changes in filament processivity affect force production. We considered a simple force-generating system consisting of an ensemble of N_{heads} motors building force on a single actin filament anchored by its barbed end to an elastic spring with a stiffness K that represented compliance of the surrounding network (Fig. 2.8a). We varied N_{heads} or $\rho_d(0)$ to tune filaments through the transition from weak attachment to processive engagement and monitored force buildup. As expected, highly processive ensembles built force steadily to the

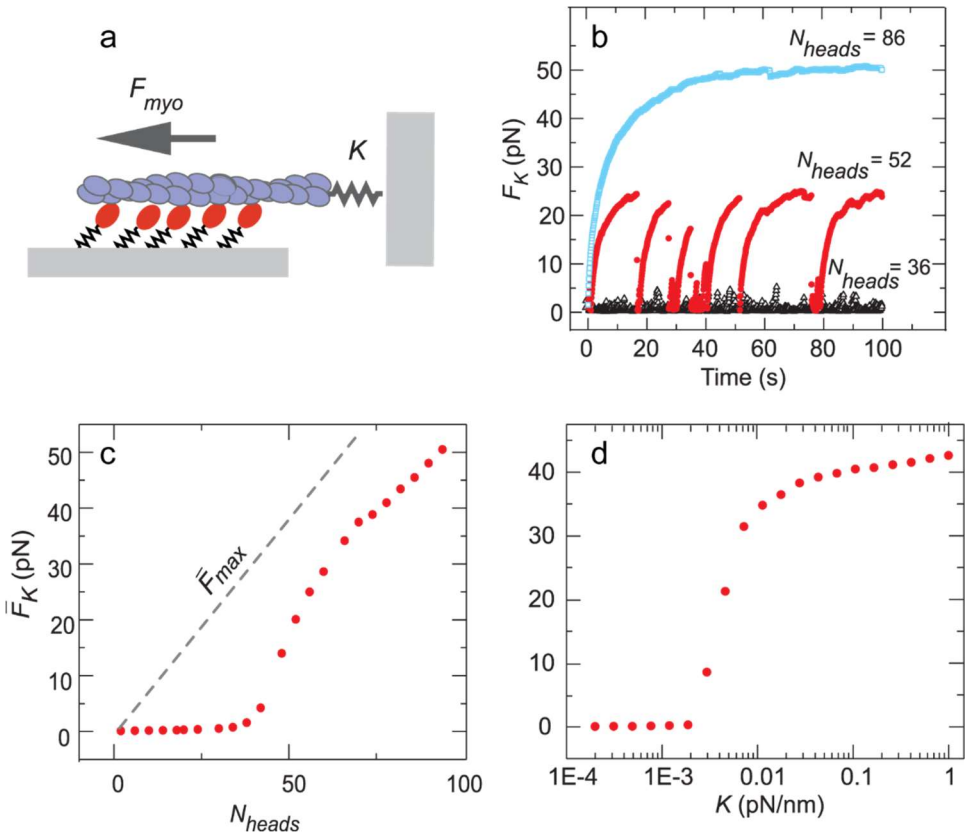

Figure 2.8 Myosin filament size and actin stiffness determined the magnitude and stability of force generation. (a) Simulations were arranged with fixed myosin heads building force on F-actin anchored to a spring with spring constant K. (b) Increasing the size of the myosin filament produced a transition from transient force build up and release to stable force maintenance. Each curve is from a single simulation. (c) The average force on the spring for different values of N_{heads}. (d) A sharp increase of the average force was also produced with increasing K. Parameter values in (b) and (c): $\rho_d(0) = 0.05$ ($k_{on} = 10\ s^{-1}$, $k_{off}(0)=191$) $K = 0.02$ pN/nm, (d): $\rho_d(0) = 0.05$ ($k_{on} = 10\ s^{-1}$, $k_{off}(0) = 191$), $N_{heads} = 74$. Each point in (c) and (d) is the average of 10000 values from 10 independent simulations of 100 s. The standard error of the forces was smaller than the data points.

maximum stall force, F_{max} (Fig. 2.8b and 2.9a, blue squares). At intermediate processivities, the initial rate of force buildup was similar but the filaments detached before reaching F_{max} (Fig. 2.8b and 2.9a, red circles). At the smallest values of N_{heads} or $\rho_d(0)$, no force was built (Fig. 2.8b and 2.9a, open black triangles).

Plotting the average force generated by myosin filaments, $\bar{F}_K$, revealed a surprisingly sharp dependence on N_{heads} (Fig. 2.8c) and $\rho_d(0)$ (Fig. 2.9c). In both cases, the average force remained

approximately zero up to a threshold value, then increased rapidly with N_{heads} or $\rho_d(0)$ to approach the average myosin filament stall force, $\bar{F}_{max}$, given by Eqn (3).

We observed a similarly sharp dependence of force buildup on network stiffness K. Reducing K produced a transition from stable force generation to intermittent force build up and release and finally to complete inhibition of force generation (Fig. 2.9b). Plotting $\bar{F}_K$ versus stiffness revealed a sharp transition from ~ 0 to maximal force for a ~4-fold change in K (Fig. 2.8d). The value of K at which this transition occurred depended on both N_{heads} and $\rho_d(0)$.

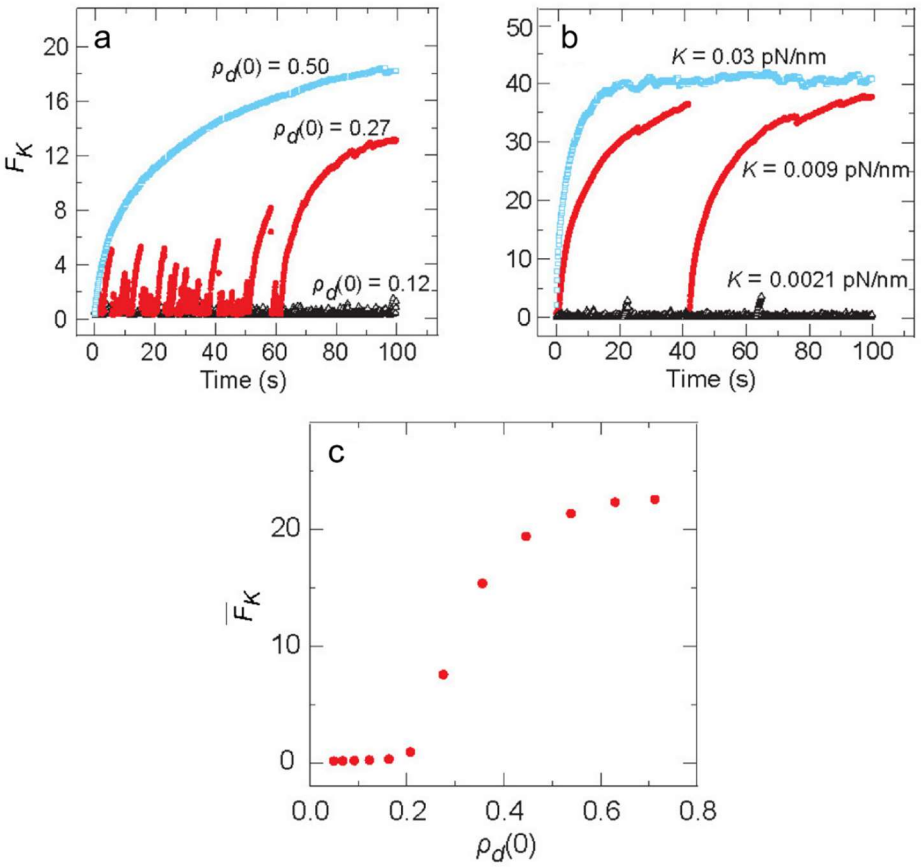

Figure 2.9 Dependence of force buildup on unloaded duty ratio ρd(0) and environmental stiffness K. (A) and (B) The force F_K generated by the motor cluster against an external elastic load over time for different values of $\rho_d(0)$ (A) or K (B). (C) Average value of F_K measured as a function of $\rho_d(0)$. Each point is the average of 10000 values from 10 independent simulations of 100 s. Parameter values in (A): k_{on} = 10 s^{-1}, N_{heads} = 10, K = 0.02 pN/nm, (B): $\rho_d(0)$ = 0.05 (k_{on} = 10 s^{-1}, $k_{off}(0)$ = 191 s^{-1}), N_{heads} = 74, and (C): k_{on} = 10 s^{-1}, N_{heads} = 10, K = 0.02 pN/nm.

The sharp dependence of average force on motor properties or network stiffness reflects a competition between timescales of myosin attachment and force buildup. Intuitively, a sharp increase in force output should occur when attachment time exceeds the time to build the maximum (i.e. stall) force. Thus, in addition to their effects on attachment time, we must understand how motor properties and network stiffness control the rate of force buildup.

Determinants of characteristic time scale of force buildup

To this end, we varied k_{on}, k_{off}, and N_{heads} and measured the time required to build 70% of the maximum force (t_{build}) as a function of $\bar{F}_{\max}$, $\bar{V}_{max,}$ and K. As expected, faster motors built force more rapidly such that t_{build} scaled linearly with $1/\bar{V}_{max}$ (Fig. 2.10a). For a constant motor speed, t_{build} should also increase in proportion to the number of steps required to reach the stall force; consistent with this, t_{build} was directly proportional to $\bar{F}_{max}$ (Fig. 2.10a) and inversely proportional to K (Fig. 2.10b). Combining these, we observed a single scaling relationship for t_{build} as a function of all three parameters (Fig.2.10c):

$$t_{build} \sim \frac{\bar{F}_{max}}{K\bar{V}_{max}} \tag{4}$$

Interestingly, we observed a similar scaling when we removed the force dependence of myosin release, albeit with a lower slope (Fig. 2.10C, dark blue diamonds). Thus myosin motors build force more quickly on stiffer substrates regardless of the exact mechanochemistry. This suggests that force-dependent kinetics may not be required for experimentally observed increases in the rate

of force generation with external stiffness of contractile cells as has been previously assumed (50-52).

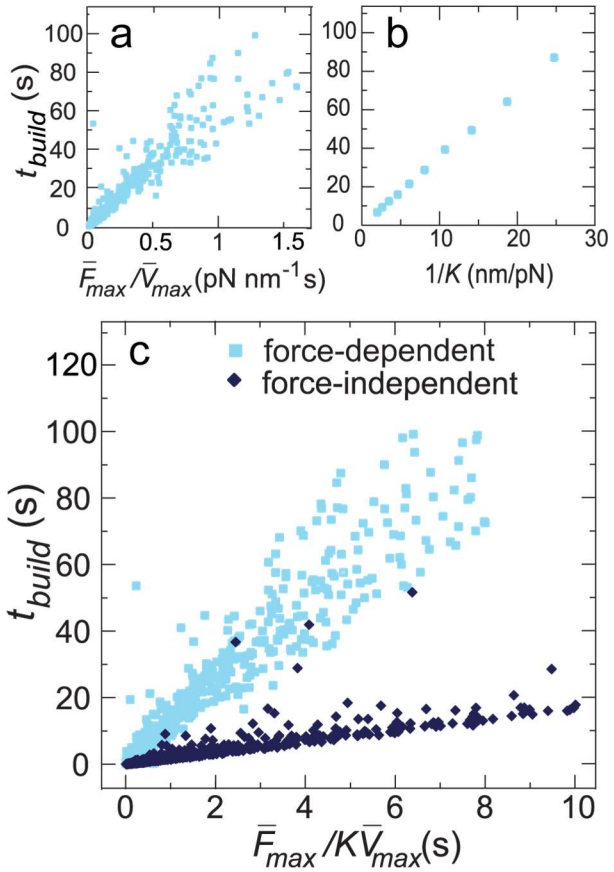

Figure 2.10 The characteristic time required for processive motors to build to stall, t_{build}, scaled as $\bar{F}_{max}\bar{V}_{max}^{-1}K^{-1}$. (a) A linear increase of t_{build} was observed with $\bar{F}_{max}/\bar{V}_{max}$ with K = 0.01 pN/nm. The values of $k_{\text{off}}(0)$, k_{on}, and N_{heads} were varied from 10 s^{-1} to 191 s^{-1}, 1 s^{-1} to 10 s^{-1}, and 6 to 600 respectively. (b) t_{build} also increased linearly with 1/K. Parameter values: N_{heads} = 50, $\rho_{\text{d}}(0)$ = 0.05 (k_{on} = 10 s^{-1} and $k_{\text{off}}(0)$ =191 s^{-1}). (c) The final scaling relationship for both force-dependent and force-independent motors. The same ranges of $k_{\text{off}}(0)$, k_{on}, and N_{heads} from (a) were used with K ranging from 0.001 to 1 pN/nm. Each data point is from a single simulation of 200 s.

Force-dependent myosin kinetics produced a switch-like transition from non-processive to processive force generation

The above analysis shows that motor properties and network stiffness control force output by controlling the balance of t_{attach} and t_{build}. In addition, given force-dependent release kinetics, t_{attach} should increase during force buildup, and this increase could sharpen the response of force output

to N_{heads} or duty ratio or external stiffness. For myosin filaments building force against an elastic load, the mean attachment time ($\bar{t}_{attach}$) should fall between the two extreme values measured under unloaded or stalled conditions (Fig. 2.6b). Indeed, for relatively small myosin filaments (Fig. 2.11a, open squares), values of $\bar{t}_{attach}$ resembled those of unloaded motors (Fig. 2.11a, black line). Increasing N_{heads} produced a sharp, faster-than-exponential increase in $\bar{t}_{attach}$ (Fig. 2.11a, open squares) that coincided with a sharp increase in average force (Fig. 2.11b, open squares). Absent

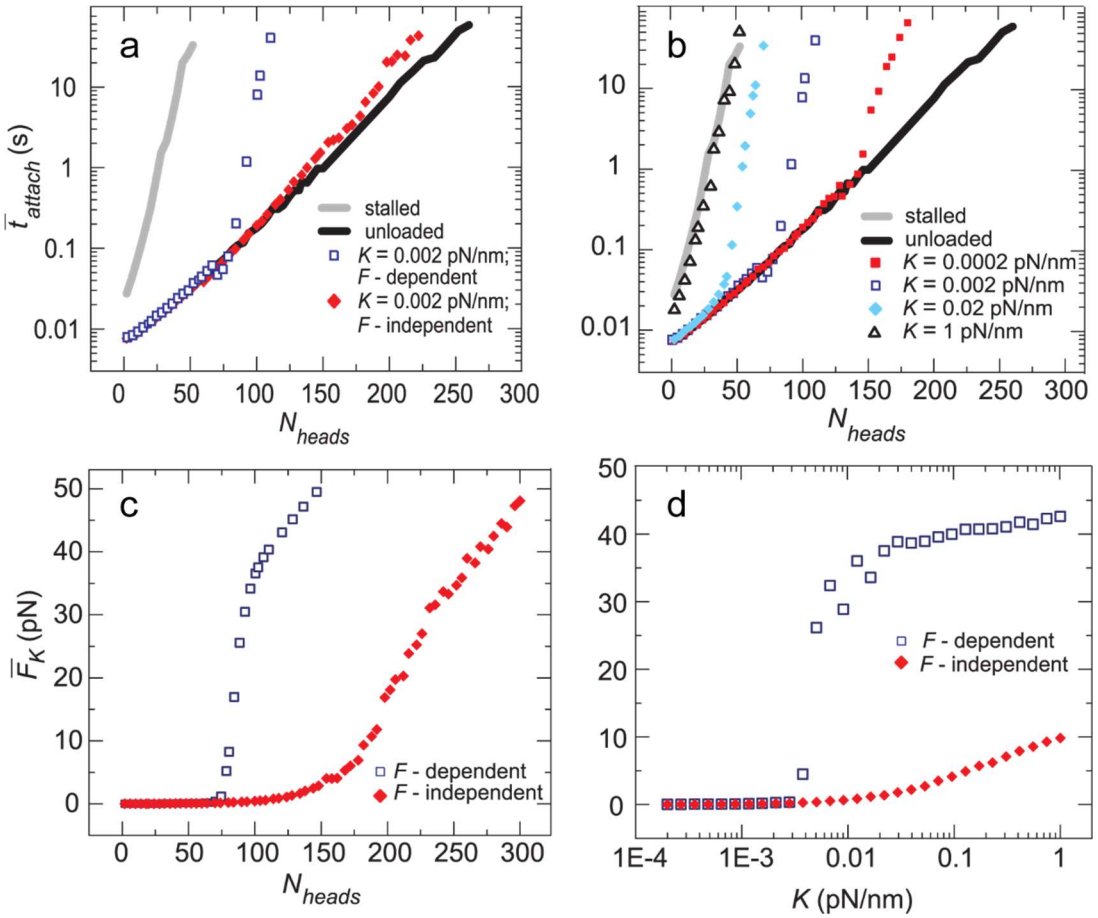

Figure 2.11 Force-dependent myosin kinetics produced a switch-like transition into processive state (a) The average attached interval, t_{attach}, increased with N_{heads} for unloaded, stalled, and spring-loaded actin filaments. For the spring-loaded case, curves in which force-dependence of k_{off} was either included or neglected are shown. (b) Average force output in the spring-loaded cases from (a). (c) The steep increase of t_{attach} for spring-loaded actin filaments was shifted with varying K. (d) Force production at a single value of N_{heads} was sharply dependent on stiffness when k_{off} was force-dependent. Force-independent motors showed a weaker dependence on K. N_{heads} = 50. In all panels, $\rho_d(0)$ = 0.05 (k_{on} = 10 s^{-1} and $k_{off}(0)$ = 191 s^{-1}). Each data point represents an average over 15 200 s simulations. The standard error was smaller than the size of the data points.

force-dependent kinetics, both the faster-than-exponential increase in $\bar{t}_{attach}$ and the sharp increase in force were completely abolished, and the dependence of mean attachment times on N_{heads} was very similar to that of unloaded motor ensembles (compare red diamonds vs. dark blue open squares in Fig. 2.11a, b). Thus, the number of motors required to generate a given level of force was significantly higher for motors lacking force-dependent kinetics and the rate of force increase with N_{heads} at a threshold value was lower.

These data reveal how force-dependent kinetics mediate positive feedback in which force buildup promotes increased attachment and further force buildup. This feedback sharpens the effect of increasing duty ratio or filament size such that small increases in either quantity above threshold values caused a rapid transition from a state in which transient attachments produced little force to one in which force was built and maintained over long timescales. As a consequence of this feedback, large force fluctuations depicted by the red circles in Fig. 2.8b, 2.9a, and 2.9b occurred only within narrow ranges of N_{heads} or the motor duty ratio.

Mechanical cues regulate the switch to processive force generation

The same positive feedback could also explain the increased sensitivity of force production to environmental stiffness, as shown in Fig. 2.8d, because motor filaments will build force faster on stiffer substrates and thus engage positive feedback more readily. Consistent with this, the sharp increase in average force with increasing network stiffness was completely abolished in motor filaments lacking force-dependent kinetics (red vs. dark blue traces in Fig. 2.11d).

Moreover, we found that different levels of external stiffness shifted the threshold filament size (Fig. 2.11c) or duty ratio (not shown) required to engage positive feedback. In very stiff environments (i.e when K exceeds the myosin cross-bridge stiffness of 0.7 pN/nm), $\bar{t}_{attach}$ was

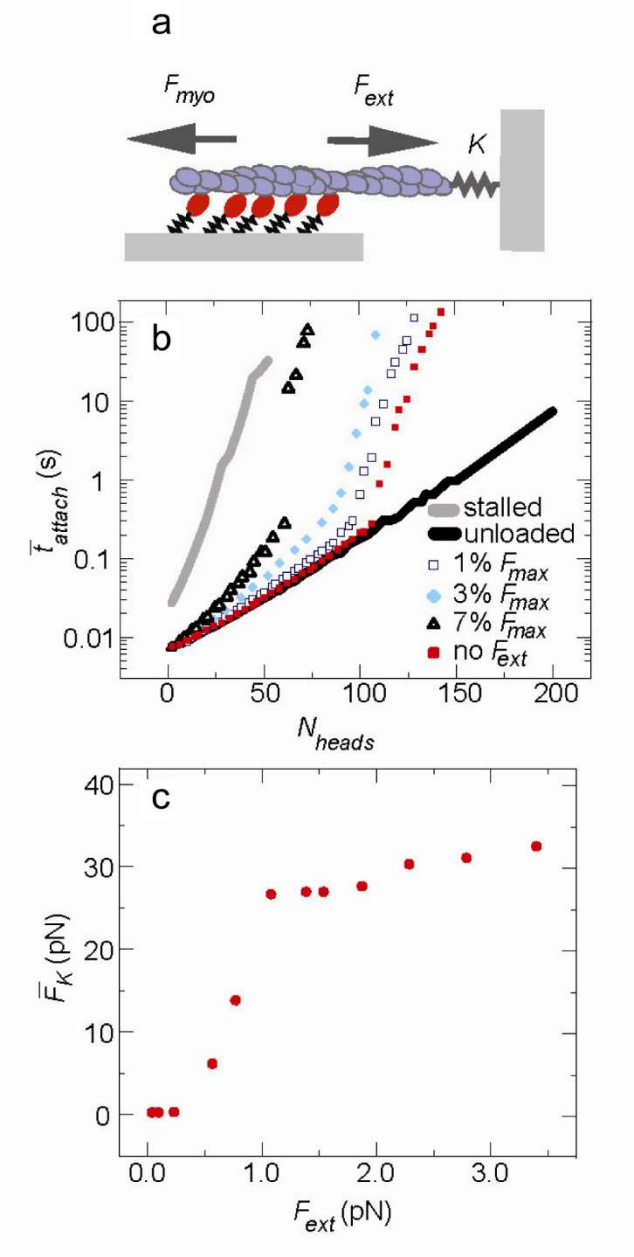

Figure 2.12 A small constant force superimposed on a linear load can trigger processive force generation. (A) Schematic of myosin motors building force on a linear spring against a small opposing force F_{ext}. (B) Dependence of the average attached time of the actin filament on N_{heads} for different values of F_{ext}. (C) Increase in the mean force generated against the elastic spring with increasing values of F_{ext}. Parameter values in (B): $\rho_d(0) = 0.05$ ($k_{on} = 10$ s^{-1} and $k_{off}(0) = 191$ s^{-1}), $K = 0.0006$ pN/nm (C): $\rho_d(0) = 0.05$ ($k_{on} = 10$ s^{-1} and $k_{off}(0) = 191$ s^{-1}), K=0.0006 pN/nm, $N_{heads} = 100$. Averages were taken over 15 simulations of 1000 s.

similar to that expected from stalled motors (Fig. 2.11c, gray line) because the motors reached stall very quickly (Fig. 2.11c, open triangles). In softer environments, the threshold filament size

required to engage positive feedback increased with decreasing K from N_{heads} ~1 for K = 1 pN/nm to N_{heads} ~40 for K = 0.02 pN/nm to N_{heads} ~150 for K = 0.0002 pN/nm (Fig. 2.11c).

Finally, we found that the same positive feedback could also render force production sensitive to an externally applied force, as can be seen by holding K constant and applying a small constant load (F_{ext}) to the actin filament (Fig. 2.12a). As shown in Fig. 2.12b, increasing F_{ext} from 0% to 7% of the myosin filament stall force, F_{max}, reduced the threshold filament size required to transition from non-processive to processive engagement from N_{heads} ~100 to N_{heads} ~60. Alternatively, increasing the externally applied force for fixed motor parameters and filament size produced a very sharp increase in average force over a narrow range of F_{ext}. For the motor parameters used in Fig. 2.12c, an increase in F_{ext} from 0 to 1 pN (about 5% of the stall force) produced an increase in the average force from ~0 to F_{max}. Thus, the myosin catch-bond renders force production on an elastic substrate highly responsive to relatively small variations in applied force.

Myosin II isoform performance in elastic networks

To assess the potential consequences of the behaviors described in Figs. 2.6, 2.8, 2.10, 2.11, and on different myosin II isoforms, we utilized parameters that reflected N_{heads} and enzymatic rates of skeletal muscle, non-muscle IIA, and non-muscle IIB and considered the timescales of attachment and force buildup as the environmental stiffness K was varied.

For parameters consistent with skeletal muscle myosin filaments (Table 2, Fig. 2.1), the unloaded $\bar{t}_{attach}$ was approximately 70 s. As K varied from 0.001 to 1 pN/nm, t_{build}^{fit} obtained from

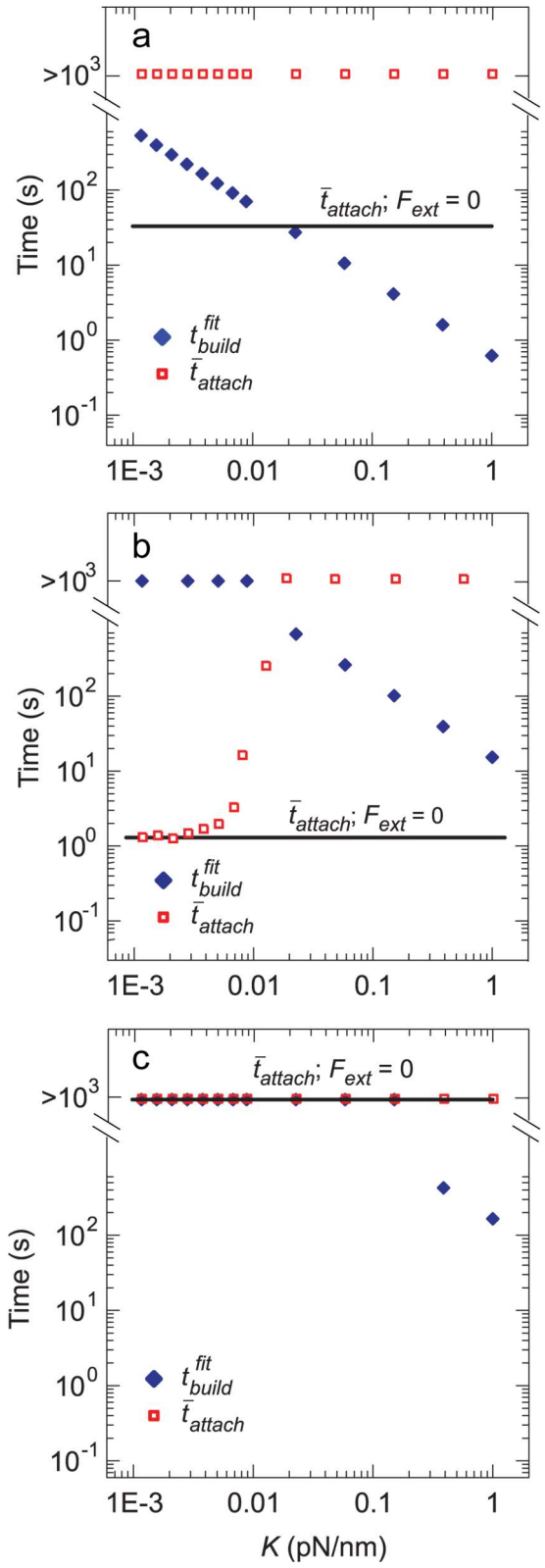

Figure 2.13 Myosin isoforms are predicted to display varying types of behavior on elastic substrates due to differences in t_{attach} and t_{build}.

Figure 2.13, continued. (a) For motor parameters that correspond to skeletal muscle myosin, the unloaded $\bar{t}_{attach}$ (solid line) was comparable to or larger than t_{build}^{fit} (diamonds), producing values of $\bar{t}_{attac}$ on spring-loaded filaments (open squares) longer than the simulation time of 1000 s for all values of *K*. (b) For parameters representative of non-muscle myosin IIA, $\bar{t}_{attach}$transitions from values much less than t_{build}^{fit} to values much greater than t_{build}^{fit} at a threshold value of *K*, leading to a sharp increase in effective force production. (c) For parameters representative of non-muscle myosin IIB type motor, both $\bar{t}_{attach}$and t_{build}^{fit} are large for all values of *K*. For all panels, the default parameters in Table 1 and isoform-specific parameters from Table 2 were used. Values of N_{heads} in (a): 500, (b): 50, (c): 50. Data points for $\bar{t}_{attac}$ are average values over 15 simulations of 1000 s while t_{build}^{fit} was calculated using a fit to the scaling relationship in Fig 4.

the scaling relationship of Fig. 2.10 decreased from ≈ 400 s to 0.5 s, while $\bar{t}_{attach}$ rapidly increased to values exceeding our simulation time of 1000 s (Fig 2.13a). Thus, the combination of the large filament size and high speed of skeletal muscle myosin II allowed for rapid and stable build up of force over a wide range of stiffness.

Using motor parameters and filament size appropriate for non-muscle myosin IIB yielded stable attachment ($\bar{t}_{attach}$ > 1000 s) in unloaded conditions for all values of *K* (Fig. 2.13c). However, t_{build}^{fit} also was >1000 s for *K* < 0.1 pN/nm, decreasing to ~100 s only for *K* > 1 pN/nm. These data suggest that myosin IIB is well-tuned to function as a high-affinity cross-linker over a wide range of environmental stiffness and force, as has been speculated previously (26, 27). However the exceedingly slow force buildup time suggests that myosin IIB will be very ineffective at generating force against actin networks that turn over on timescales relevant for rapid morphogenic change (1-100 s; see discussion).

Intriguingly, when we chose parameters appropriate for non-muscle myosin IIA filaments, our simulations predicted qualitatively distinct behaviors at low and high *K* (Fig. 2.13b). When *K*

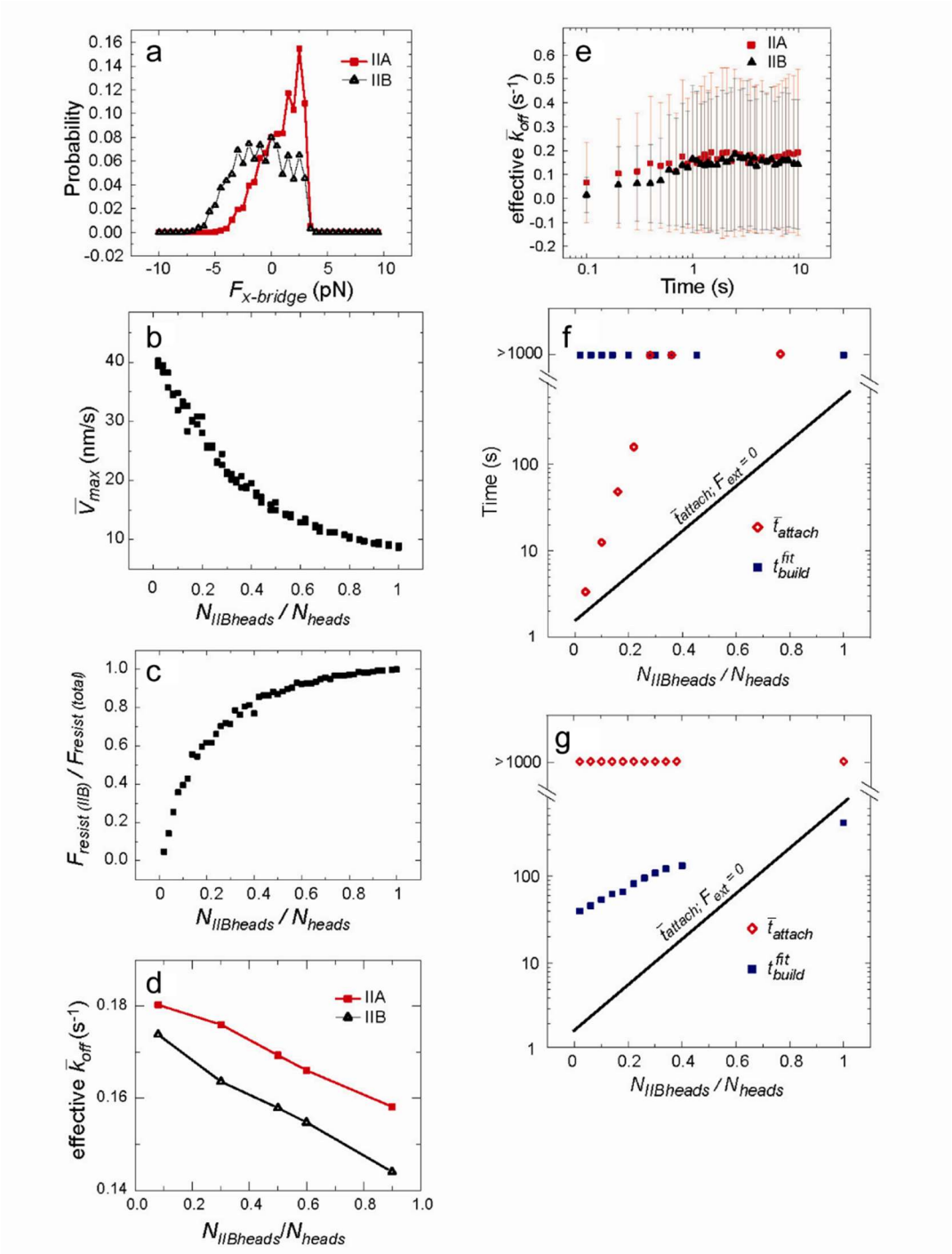

Figure 2.14 Coassembly of non-muscle myosin IIA and IIB (a) During unloaded gliding, isoforms show different distribution of crossbridge forces in mixed filament where $N_{\text{IIAheads}} = N_{\text{IIBheads}} = 25$. (b) Unloaded velocity decreases with increasing fraction of NM IIB. (c) Fraction of the total resistive forces sustained by NM IIB motors in (b). (d) Increasing the fraction of NM IIB decreases the measured cycling rate, or effective $\bar{k}_{off}$. (e) The effective $\bar{k}_{off}$ where

Figure 2.14, continued. $N_{IIAheads} = N_{IIBheads} = 25$ reaches a steady state on a similar timescale as velocities or forces in Fig. 2.3, 2.4b, and 2.4c. (f) and (g) Average t_{attach} and t_{build} on elastic load with $K = 0.004$ pN/nm (f) and $K = 0.4$ pN/nm (g). In all panels, the total $N_{heads} = 50$. In (a)-(c), 1000 data points were averaged over 100 s of simulation time. In (d), the effective k_{off} was averaged over 200 40 s simulations while (e) is the average of 200 10 s simulations. In (f) and (g), data points for t_{attach} are average values over 15 simulations of 1000 s while t_{build}^{fit} was calculated using a fit to the scaling relationship in Fig. 4. Error bars represent standard deviations.

is large, myosin IIA filaments are predicted to bind processively at stall. However, for $K < 0.01$ pN/nm, the time required to build force was too long to engage positive feedback and switch to stable attachment, so the attachment time remained quite short ($\bar{t}_{attach} < 1$ s). Around 0.01 pN/nm, a sharp transition to processive force build up occurred as t_{build}^{fit} decreased from 500 to 1 s with a concomitant increase in $\bar{t}_{attach}$. These results suggest that myosin IIA may be poised to serve as a low affinity cross-linker at low stiffness but a processive force generator at high stiffness.

Finally, we assessed the functional consequences of mixing Myosin II isoforms within individual filaments (105) focusing on mixtures of non-muscle Myosin IIA and IIB, and holding filament size constant. Not surprisingly, the model predicted values for filament processivity, stall force and filament gliding speeds intermediate between those of "pure" IIA and IIB filaments; the latter reflects a competition between the slower IIB and faster IIA motors that is mitigated by force-dependent release kinetics (Fig 2.14a-e). Both t_{build}^{fit} and $\bar{t}_{attach}$ are predicted to increase with increasing fraction of IIB motors. At low K where t_{build}^{fit} is already prohibitively high for force buildup, the simulations predict a sharp increase in $\bar{t}_{attach}$ implying a sharp increase in crosslinking affinity (Fig 2.14e). At higher K where the filament processivity is high (i.e. above the force buildup transition in Fig. 2.13b), we observed a modest increase in t_{build}^{fit} with increasing fractions of IIB (Fig 2.14g). Thus, small to moderate amounts of IIB in a composite filament could yield large increases in affinity at low K with relatively minor increases of force buildup time for the

same filament at higher K. These mixed filaments still allow for faster force buildup than filaments composed entirely of myosin IIB.

2.4 Discussion

Cross-bridge models have been used extensively to model force generation by skeletal muscle contracting against a constant load (7, 49, 85-89). Here, we used this approach to examine how the production and maintenance of force is influenced by filament size, motor duty ratio, and actin gliding velocity that vary amongst myosin II isoforms as well as force dependence of the motor duty cycle that all isoforms possess. We found that the amount of force generated against loads of varying stiffness is regulated by the relative timescales of force buildup and force relaxation due to myosin filament detachment and characterized the parameters controlling these two quantities.

These results yield insight into how cellular contractility may be regulated by internal or external mechanics or the presence of myosin isoforms with varying properties. For example, the mechanical stiffness, K, affects the time to build force through $t_{build} \sim \bar{F}_{max}/K^*\bar{V}_{max}$. At small K, this timescale may limit the amount of force that is built before force relaxation, due to myosin filament detachment or other mechanisms, occurs. However, if this timescale is sufficiently small compared to relaxation times, myosin filaments will generate their stall force and further increases in K will not affect force output. In dynamic cellular networks, other processes such as actin cross-linker unbinding (106, 107) or F-actin turnover (42) may help to set the timescale of force relaxation.

Therefore, mechanosensitivity of force generation does not require catch-bond kinetics as has been assumed in previous models (50-52). However, the catch-bond allows the timescale of

myosin attachment, t_{attach}, to depend on external force or stiffness. In our simulations, this created positive feedback between generated force and myosin filament attachment. As a result, myosin filaments could transition from a low force-generating state ($t_{build} >> t_{attach}$) to a more processive state, and the dependence of force output on K was sharper when the catch-bond was included. A similar sharp transition also occurred with small changes myosin filament parameters. We expect that there are many ways in which cells could tune myosin filaments into a regime where small forces engage this feedback and effectively turn on contractility. The size and density of myosin filaments, affinity of myosin for different actin network geometries, and actin network viscoelasticity may all vary significantly and be regulated spatiotemporally. For example, the nonlinear elasticity of actin networks is highly dependent on internal or external prestress and network connectivity (108). Relaxation due to crosslinker unbinding (106, 107) or actin turnover (42) may occur on the order of 1-100 s.

We predict that parameter values spanned by different isoforms of myosin II could produce distinct patterns of force generation in environments with varying stiffness due to these effects of relative timescales. Motor clusters representative of skeletal muscle myosin processively built force over the entire range of stiffness we explored. In contrast, we expect the nonmuscle myosin isoforms to show greater selectivity for stiffness or other mechanical signals. In the case of a nonmuscle IIA-like filament, the attachment time and average force showed a steep increase with increasing stiffness consistent with the positive feedback described above. For myosin IIB, the attachment time even for an unloaded filament was over 1000 s. However, force generation on soft substrates is likely limited due to the long time scale of force buildup, and in this regime the filaments may primarily function as actin cross-linkers. While it has been proposed that the non-muscle myosin IIA and non-muscle myosin IIB duty cycles were better tuned for tension

generation and tension maintenance respectively (26, 27), to our knowledge this is the first example demonstrating this behavior with experimentally measured parameters and revealing its dependence on stiffness. Recent work has shown co-polymerization of non-muscle myosin isoforms in vivo (105), which may serve as an additional regulatory mechanism to construct myosin filaments with varying biophysical properties (Fig. 2.14).

Finally, our results have implications for coarse-graining of myosin activity in simulations and analytical work. Alternative representations of myosin activity as either time-independent force dipoles (109) or force dipoles that transiently pull and release (110) within a continuum elastic or fluid medium have been used for applications such as predicting the strain field from interacting dipoles and mechanical properties of active networks. Our results suggest that the appropriate representation will depend on the myosin isoform and the mechanical context in which the motor operates. More detailed representations that allow the dipole kicking rate to depend on force may be essential to capture force-dependent dynamics that underlie large-scale deformations of an actomyosin network (111). How motor properties influence an actomyosin network's ability to produce force or change its shape, or how they may modulate such activity if the network is subjected to external force or tethering to an external substrate are interesting questions for future study.

Chapter 3 Filament rigidity and connectivity tune the deformation modes of active biopolymer networks

3.1 Introduction

Assemblies of semi-flexible filaments and molecular motors are active materials (18) that drive many physiological processes such as muscle contraction (1), cytokinesis (2), cytoplasmic transport (3), and chromosome segregation (112). To actuate these processes, the nanometer-scale displacements of motors and local deformation and sliding of filaments must give rise to coordinated mesoscale deformations of such active materials. These mesoscale dynamics result in the transmission of cellular-scale forces with different directions (e.g., contractile or extensile) and shapes (e.g., isotropic or anisotropic) which, in turn, result in shape changes at cellular and ultimately tissue length scales. Characterizing deformations in active networks of different molecular compositions is a much needed first step toward understanding complex force transmission and shape changes observed in cells and tissues.

Understanding how assemblies of filaments and motors produce a net contractile or extensile force has been extensively explored theoretically (59-62, 65, 66, 69). Experimentally, *in vitro* networks constructed from actin filaments and myosin II motors are robustly contractile (53-56). By contrast, systems of microtubules and molecular motors are either extensile (57-60) or contractile (113, 114). One difference between these two active materials is that microtubules are significantly more rigid than actin. Recent work has shown that contractile stress can be generated via motor stress-induced filament buckling (55, 65, 66), indicating an important role for filament rigidity. Alternative microscopic mechanisms to generate extensile or contractile stress by motor-

mediated sliding of rigid filaments have also been proposed (59, 61, 62, 69). The network-scale consequences of these different force-generating mechanisms have not been explored.

Deformations within active matter can be characterized beyond whether they are contractile or extensile. For example, network-scale force transmission is known to be affected by network connectivity, which regulates the length scale of contraction (53, 54, 67, 71, 111). Moreover, recent data suggests that disordered actomyosin networks contract isotropically (115, 116). *In vivo*, anisotropic contraction dominates in cell division and muscle contraction (5). Understanding how to control the prevalence of isotropic versus anisotropic deformations will further our understanding of how these contractile deformations are regulated *in vivo*.

Here, we directly vary the stiffness and connectivity of filaments within an *in vitro* biopolymer network through cross-linking and investigate the effects on network deformation. Through quantitative analysis of experimental data, we determine that these mechanical properties affect the anisotropy and contractility of deformations caused by the motor protein myosin II. Networks composed of semi-flexible filaments that can be buckled by motor stresses exhibit robust biaxial contraction. Increasing the filament rigidity results in uniaxial deformations, the direction of which is regulated by cross-linker density. Extensile deformations are generated at low cross-linker density and contractile deformations occur at high cross-linker density. Using agent-based simulations, we identify the microscopic deformation modes underlying these observations and find that forces are transmitted uniaxially by rigid filaments that slide and do not buckle. Together, our results indicate how motor-filament interactions can generate forces that result in either extensile or contractile deformations, which vary in shape depending on the filament rigidity and

connectivity. From our experimental and simulation data, we propose a phase space of active matter constructed from motors and filaments.

3.2 Methods

Protein purification

Actin was purified from rabbit acetone powder (Pel-Freez Biologicals, Rogers, AR) with a protocol derived from (117) and stored as a monomer in G-buffer (2 mM Tris HCl pH 8.0, 0.2 mM ATP, 0.2 mM $CaCl_2$, 0.2 mM DTT, 0.005% NaN_3). Fluorescent labeling of actin was done with a tetramethylrhodamine-6-maleimide dye (Life Technologies, Carlsbad, CA). Skeletal muscle myosin II was purified from chicken breast (118) and labeled with Alexa-642 maleimide (Life Technologies, Carlsbad, CA) (119). Filamin was purified from chicken gizzard (120). Fascin was purified using a GST-tagged construct (121) and Dave Kovar lab, University of Chicago). Purification was done using a glutathione sepharose column (GE Healthcare Life Sciences). The GST tag was then cleaved with thrombin (GST Healthcare Life Sciences) and separated by chromatography (Hi-Trap Q column; GE Healthcare Life Sciences).

Microscopy sample preparation

The coverslip surface was passivated against non-specific adhesion of protein with a surfactant layer, either a lipid bilayer (122) or a fluorinated oil-surfactant layer (57). To prepare a lipid bilayer, coverslips (#1.5, Fisherbrand) were rinsed with water and ethanol, then exposed to UV-ozone for 20 minutes. The sample chamber was assembled by anchoring a glass cylinder (cat# 3166-10; Corning Life Sciences, Corning, NY) to the coverslip with vacuum grease. This was

filled with vesicle buffer (10 mM phosphate buffer, pH 7.5, 140 mM sodium chloride) and DOPC vesicles (1,2-dioleoyl-*sn*-glycero-3-phosphocholine, Avanti Polar Lipids, Alabaster, AL) were added to a concentration of 100 μM and incubated for 15 minutes to allow bilayer formation. To prepare the oil-surfactant surface, PFPE-PEG-PFPE surfactant (cat # 008, RAN Biotechnologies, Beverly, MA) was dissolved to a concentration of 2% w/w in Novec-7500 Engineered Fluid (3M, St Paul, MN). Coverslips were cleaned by sonication in water and ethanol, immersed in a 2% v/v solution of triethoxy(octyl)silane (cat# 440213; Sigma-Aldrich, St. Louis, MO) in isopropanol, and rinsed thoroughly to produce a hydrophobic surface. To constrain the oil to a small region and prevent seeping and flow from the chamber edges, a 2x2 mm Teflon mask was placed on the coverslip before exposing the coverslip to UV/ozone for 10 minutes. This removed the hydrophobic silane treatment from all surrounding areas of the coverslip. The sample chamber was then constructed, similarly as with the bilayer surface, by adhering a glass cylinder to the coverslip using epoxy. The surface of the coverslip within the cylinder was coated with the oil-surfactant solution, and the actin polymerization mixture was immediately added.

The actin polymerization mixture consisted of an oxygen scavenging system to prevent photobleaching (4.5 mg/mL glucose, 2.7 mg/mL glucose oxidase (cat#345486, Calbiochem, Billerica, MA), 1700 units/mL catalase (cat#02071, Sigma, St. Louis, MO), and 0.5 v/v % β-mercaptoethanol), and 0.3% w/w 15 cP methylcellulose (55) in 1x F-buffer (10 mM imidazole, pH 7.5, 1 mM MgCl2, 50 mM KCl, 0.2 mM EGTA, 4 mM ATP). Actin from frozen stocks in G-buffer (above) was added to a final concentration of 1 μM with a ratio of 1:10 TMR-maleimide labeled:unlabeled actin monomer. Polymerization of actin was allowed to proceed for 30 minutes. For bundled samples, fascin stored in 20 mM Tris-HCl, pH 8, 10% glycerol, 100 mM NaCl, 0.2 mM EDTA, 0.01% NaN_3 was then added at a ratio of 1:10 fascin:actin monomer and allowed to

form bundles for 20 minutes. Similarly, filamin (10 mM Tris-HCl, pH 7.4, 1 mM EDTA, 1 mM DTT, 2 mM $MgCl_2$, 120 mM NaCl) was added at a ratio of 1:500 filamin: actin monomer and allowed to crosslink for 20 minutes. Monomeric myosin II was polymerized into myosin filaments separately in the same buffer conditions for 10 minutes and added at a ratio of 1:13 myosin monomer:actin monomer.

Fluorescence microscopy

Images were obtained using an inverted microscope (Eclipse Ti-E; Nikon, Melville, NY) with a spinning disk confocal head (CSU-X; Yokagawa Electric, Musashino, Tokyo, Japan) and CMOS camera (Zyla-4.2-USB3; Andor, Belfast, UK). A 40x 1.15 NA water-immersion objective (Apo LWD; Nikon) was used for all imaging. Images were collected every 1 s using 568 nm and 647 nm excitation for the actin and myosin respectively. Image acquisition was under automated control by Metamorph (Molecular Devices, Sunnyvale, CA).

Image Analysis

Images were aligned using the StackReg (http://bigwww.epfl.ch/thevenaz/stackreg/) (123) plugin of ImageJ (https://imagej.nih.gov/ij/) (124) to remove drift. Background intensity was subtracted using the built-in Subtract Background plugin of ImageJ. The myosin particle density was calculated in ImageJ and actin velocity vectors were calculated using particle imaging velocimetry software (http://www.oceanwave.jp/softwares/mpiv/). The grid size used for PIV

vector calculation was 2.4 μm except for the systematic variation in Fig. 3.12. All further analysis was done using custom Matlab scripts.

All experimental image analysis plots that report values at different times were smoothed such that each data point represents the average over overlapping 20 s time windows. The values of the contractile moment at different length scales in Fig. 3.1j, and Fig. 3.10d were averaged for 30 s starting with the time points of maximal magnitude of $<\nabla \cdot \vec{v}_{act}>$ given by the asterisks in Fig. 3.1i and Fig. 3.10c. The rescaling of quantities in Fig. 3.6 and Fig. 3.7 was done such that their range spans from 0 to 1, e.g., $l_{corr} = \frac{L_{corr} - min(L_{corr})}{\max(L_{corr})}$.

Simulation methods

We used AFiNeS, a software package that we developed for simulating active polymer networks (28), to systematically vary actin flexibility and cross-linker density in two-dimensional networks of F-actin, myosin, and cross-linkers. These components were initially placed at random locations in a 50 μm × 50 μm box with periodic boundary conditions and evolved via overdamped Langevin dynamics for 200 s. We ran four replicates of 77 simulations, each with different crosslink density (ρ_{xl}) varying between 0 and 1 μm^{-2} and filament rigidity (κ_B) varying between 0 and 1 $pN\mu m^2$. The divergence calculation in Fig. 3.8c is weighted by the local actin density

because the experimental PIV method does not calculate vectors at locations below a threshold actin density.

3.3 Results

Networks of cross-linked rigid bundles are contractile with a short correlation length

To investigate the role of filament rigidity in active motor-filament networks, we construct a quasi-two-dimensional (quasi-2D) layer of actin *in vitro* by polymerization of 1 μM monomeric actin in the presence of a depletion agent to crowd actin filaments near a passivated surface (Fig. 3.1a) (55, 57). To increase filament rigidity, we add 0.1 μM of the actin cross-linker fascin, which constructs bundles of ~8 ± 7 actin filaments (Fig. 3.2). Actin filaments are polar, and their barbed ends are uniformly directed within fascin bundles (125). Fascin bundles are thus polar like single actin filaments but are much more rigid (Fig. 3.1b): the persistence length of bundles is estimated to be ~250 μm (126), over 10 times that of single actin filaments (64). To connect rigid bundles into networks, we add a small concentration (0.002 μM) of a second cross-linker, filamin. Filamin is a large (200 nm) and flexible cross-linker that binds overlapping bundles with varying orientations into a quasi-2D network (127, 128).

After assembling actin filaments or bundles, we add myosin II and monitor structural changes in the actin networks via fluorescence microscopy (Methods Section). Myosin II filaments (white spots) initially accumulate on the networks, and we define the time of the maximum density of

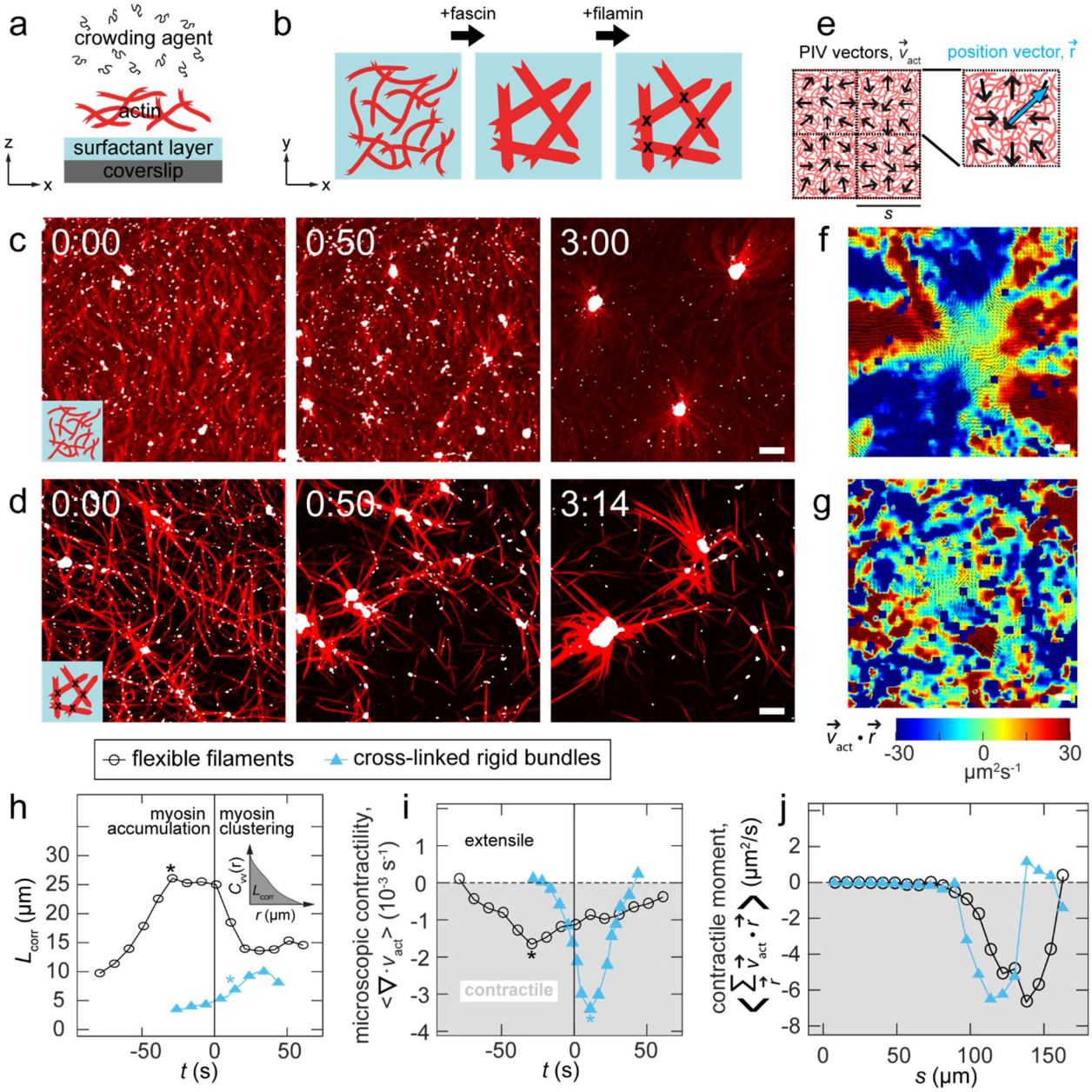

Figure 3.1 Networks of rigid bundles are contractile with a short correlation length (a) Schematic of experimental set up. Actin filaments are crowded to a surfactant-coated coverslip surface to make a dense quasi-2D layer. (b) Fascin is used to make rigid, unipolar actin bundles. Filamin is used to cross-link bundles. (c) Images of semi-flexible filaments (red) in the absence of fascin or filamin after the addition of myosin (white puncta). (d) Images of cross-linked rigid bundles formed by F-actin in the presence of fascin (1:10) and filamin (1:500) after myosin is added. (e) Particle Imaging Velocimetry (PIV) detects local motion of F-actin ($\vec{v}_{act}$, black arrows).

Figure 3.1, continued. Images are split into boxes of size *s*, and $\vec{r}$ defines a vector from the center of a box to a PIV vector within the box. (f-g) Example spatial maps of the moment of the velocity field for images at -0:40 and 0:00 of panels c & d, respectively. Negative values of $\vec{v}_{act} \cdot \vec{r}$ indicate contractile whereas positive values indicate extension. (h) The correlation length as a function of time for single filaments (open black circles) and cross-linked rigid bundles (closed blue triangles). Inset: Schematic indicating how correlation length is obtained from velocity-velocity correlation. (i) The divergence for both networks as a function of time. The asterisks in h+i indicate the time of minimal divergence, as indicated in (i). (j) The contractile moment as a function of length scale *s* for both samples. For (c)-(g), scale bars are 10 μm and time stamps are in the minutes:seconds format where 0:00 indicates the time of the maximal density of myosin puncta.

myosin puncta as $t = 0$ s (Fig. 3.3a). Myosin drives changes in actin filament or bundle orientation, position, and shape that ultimately result in the formation of actomyosin asters comprised of polarity-sorted actin filaments oriented radially with large myosin foci at the center (Fig. 3.1c and 3.1d, Fig. 3.3).

To assess the network motion leading to aster formation, we calculate local displacement vectors of the actin network between frames using particle image velocimetry (PIV) (Fig. 3.1e, Methods). To visualize propagation of contractile or extensile motion, we calculate the moment of the velocity field, $\vec{v}_{act}(\vec{r}) \cdot \vec{r}$, where $\vec{v}_{act}(\vec{r})$ is the local actin PIV vector and $\vec{r}$ is the vector from the center of a square region to the location of the PIV vector (129) (Fig. 3.1e). Locations where the moment is positive indicate local expansion from the center of the field of view whereas negative values indicate local compression. During the early stages of network reorganization before aster formation, we find that spatial propagation of inwardly or outwardly directed motion is very different in networks of semi-flexible filaments and those of cross-linked rigid bundles (Figs. 3.1f and 1g). In networks of semi-flexible filaments, motion is highly spatially correlated, with large areas contracting toward the center of the square region in the vertical direction (blue, Fig. 3.1f) and material moving outward in the horizontal direction (red, Fig. 3.1f). In contrast, in

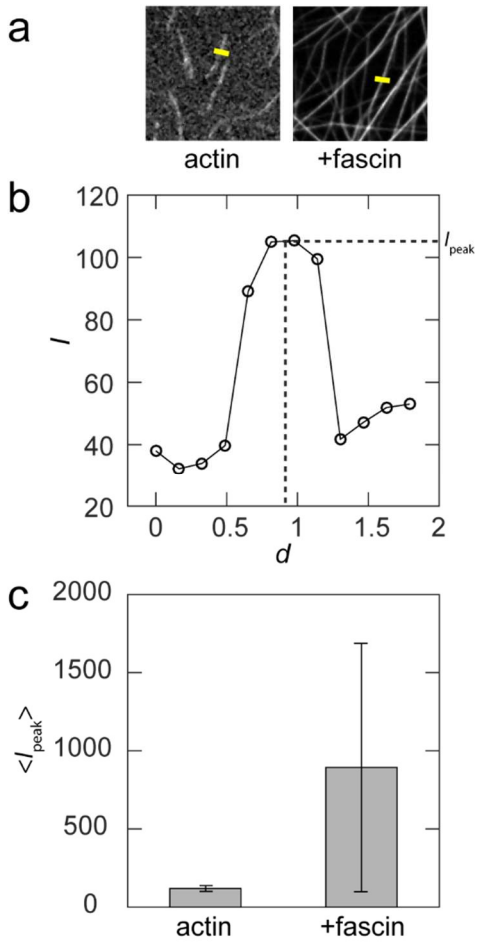

Figure 3.2 Fascin bundles contain ~ 8 actin filaments (a) Intensity scans are taken along lines perpendicular to indiviudual actin filaments (left) and rigid fasin bundles (right). (b) The resulting intensity profile has a peak intensity, I_{peak}. (c) The average value of I_{peak} for fascin bundles is approximately 8 times that of individual filaments.

the bundled network, motion is restricted to smaller, irregularly shaped contractile and extensile regions that are interspersed (Fig. 3.1g).

To characterize the length scale of the velocity field, we consider the velocity-velocity correlation function:

$$C_{vv}(r) = \frac{\langle \vec{v}_{act}(0) \cdot \vec{v}_{act}(r) \rangle}{\langle |\vec{v}_{act}(0)|^2 \rangle}$$

where r is the distance between two velocity vectors $\vec{v}_{act}$. We define a characteristic correlation length, $L_{corr,}$ as the area under the curve of $C_{vv}(r)$ at a given time (inset, Fig. 3.1h). In

both networks, L_{corr} initially increases as myosin forces accumulate in the network (Fig. 3.1h). Eventually, L_{corr} decreases as the networks break into clusters. Although L_{corr} has similar trends for both networks, its value is consistently less for the rigid bundle network than for the network of semi-flexible filaments. This is consistent with the spatial heterogeneity in the moment of the velocity field observed in the network of rigid bundles, as compared to that formed with semi-flexible filaments (Figs. 3.1f and 3.1g).

Next, we assess net contractility using two different measures. The divergence of $\vec{v}_{act}$, $\nabla \cdot \vec{v}_{act}$, is a measure of contractility on the length scale set by the spacing of PIV vectors, in this case 2.4 μm (130). Negative values indicate local contraction while positive values indicate local expansion. For networks of semi-flexible filaments, the spatial average of $\nabla \cdot \vec{v}_{act}$ is negative (Fig 3.1i, open black circles), indicating net contraction, consistent with previous reports (130). The divergence reaches a maximally negative value as myosin accumulates on the network before separation of actin into clusters, at which point local extension between clusters balances contractility to produce $\langle \nabla \cdot \vec{v}_{act} \rangle \sim 0$ s^{-1}. Similarly, the cross-linked rigid bundle network exhibits a negative divergence that returns to values near 0 s^{-1} after the onset of network coarsening at 0 s (Fig. 3.1i, filled blue triangles). Thus, the contractility is slightly enhanced in networks of rigid bundles as compared to those of semi-flexible filaments.

To characterize the length scale of contraction, we measure the contractile moment by summing $\vec{v}_{act}(\vec{r}) \cdot \vec{r}$ over non-overlapping square regions of varying side length s (Fig. 3.1j) (129). Negative values of the contractile moment indicate that contractile motion propagates across regions with this length scale (129). In both networks, $\langle \sum_{\vec{r}} \vec{v}_{act}(\vec{r}) \cdot \vec{r} \rangle$ reaches a minimum for regions of length 100 μm < s < 150 μm. Thus, contraction in both materials can propagate over

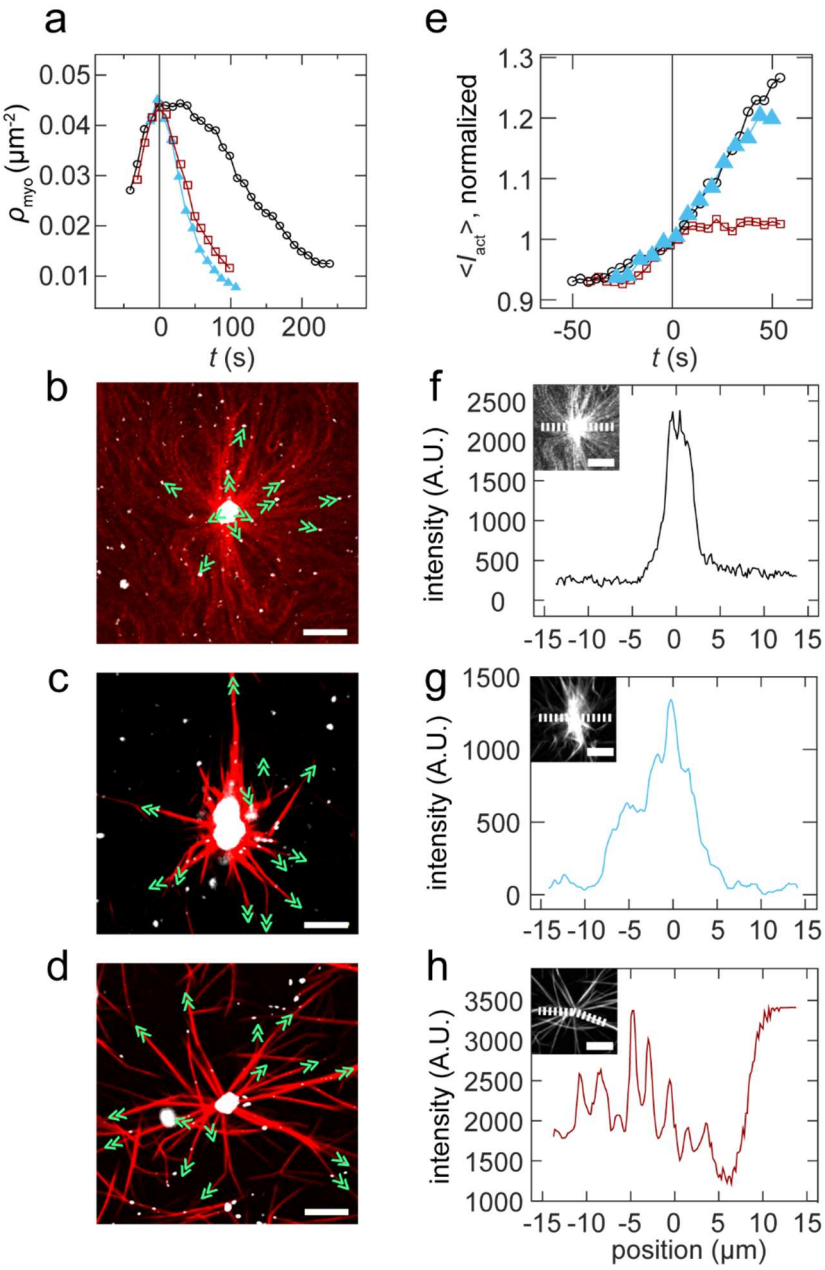

Figure 3.3 Networks form polarity-sorted asters with varying structure (a) Time $t = 0$ defines the peak myosin cluster density after myosin filaments accumulate on the surface and begin to coalesce in semi-flexible filament network (open black circles), cross-linked rigid bundles (1:10 fascin:actin, 1:500 filamin:actin, filled blue triangles), and rigid bundles without cross-links (1:10 fascin:actin open red squares). (b-d) By tracking the motion of myosin on bundles/filaments that emanate from the aster, the local polarity is assessed and marked on images with the open end of the chevron indicating the direction of motion and direction of barbed end. Aster polarity in (b) semi-flexible filament network, (c) cross-linked rigid bundles (1:10 fascin:actin, 1:500

Figure 3.3, continued. filamin:actin) and (d) rigid bundles without cross-links (1:10 fascin:actin). (e) $\langle I_{act} \rangle$ in each frame is calculated by averaging the actin over all pixels that exceed a background threshold, and then normalizing by the value at time t = 0. Densification of actin, indicated by a rise in this value, occurs in semi-flexible filament (open black circles) and cross-linked rigid bundle (filled blue triangles) while rigid bundles without cross-links are rearranged without densification (open red squares). (f)-(h) Intensity scans of clusters formed in the compressible filament (d), cross-linked rigid bundle (e) and uncross-linked rigid bundle (f) networks. As a consequence of the densification illustrated in (e), actin is highly concentrated in the center of the asters in (f) and (g). In contrast, the aster in (h) has intensity peaks diffusively spread throughout the structure. Scale bars on insets are 10 μm.

large length scales. However, the consistent picture that emerges is that the collective motions in the rigid networks occur over shorter length and time scales.

Rigidity controls the anisotropy of contractile deformations

To explore the origin of differing spatial distribution of motion within these contractile networks, we sought to characterize the local deformations. We apply a method previously used to characterize the anisotropy of forces exerted by cells (129). We consider the tensor

$$M_{ij} = \sum_{\vec{r}} v_{act}(\vec{r})_i r_j$$

where i and j denote the in-plane spatial coordinates. By diagonalizing this tensor, we can extract the principle deformation axes. The magnitudes of the eigenvalues, M_{max} and M_{min}, are the major and minor axes respectively of an ellipse characterizing the anisotropy of the deformation (Fig. 3.4a). A value of M_{min}/M_{max} of 0 indicates a completely uniaxial deformation, while a value of $M_{min}/M_{max} = 1$ indicates a completely biaxial deformation (Fig. 3.4a). For a given length scale (s = 20 μm), a distribution of M_{min}/M_{max} from deformations across the field of view is obtained at each time point (Fig. 3.4b, Fig. 3.4c). In networks of semi-flexible filaments, the distribution is clearly weighted towards biaxial deformations ($M_{min}/M_{max} > 0.5$) at all times during contraction

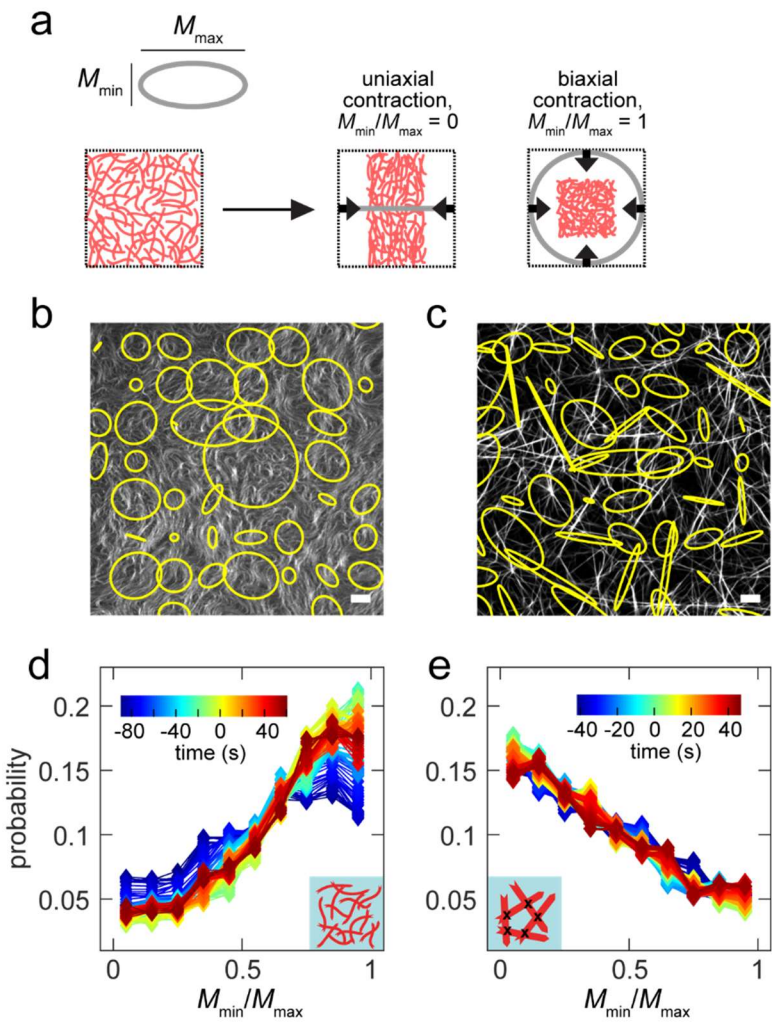

Figure 3.4 Deformations are highly biaxial and uniaxial in networks of semi-flexible filaments and rigid bundles respectively. (a) The eigenvalues of the flow dipole moment tensor, M_{min} and M_{max}, are the axes of an ellipse that characterizes the deformation anisotropy, with uniaxial and biaxial contraction illustrated. (b) and (c) Images of deformation anisotropy in networks of semi-flexible filaments (b) and rigid bundles (c). (d) and (e) Distribution of M_{min}/M_{max} at varying times (color scale) at s = 20 μm for semi-flexible filaments (d) and cross-linked rigid bundles (e).

(Fig. 3.4d). By contrast, in cross-linked rigid bundle networks, the distribution is highly weighted towards uniaxial deformations ($M_{min}/M_{max} < 0.5$) at all times (Fig. 3.4e). We find that these characteristic differences in deformation anisotropy between rigid and semi-flexible networks persist across length scales varying from s = 6 μm up to 60 μm (Fig. 3.5). To examine the effect of different deformations on correlated motion and contraction, we next consider the change in the fraction of predominately biaxial ($M_{min}/M_{max} > 0.5$) or uniaxial ($M_{min}/M_{max} < 0.5$) deformations and term these $P_{biaxial}(s)$ and $P_{uniaxial}(s) = 1 - P_{biaxial}(s)$, respectively (Fig. 3.6). We compare these quantities to the correlation length, L_{corr}, and the microscopic contractility as a function of time. Versions of these quantities that are rescaled to range from 0 to 1 are indicated by lower case letters, e.g., $p_{biaxial}$(s) and l_{corr} (see Methods). For both rigidities, either $p_{biaxial}(s)$ or $p_{uniaxial}(s)$ is

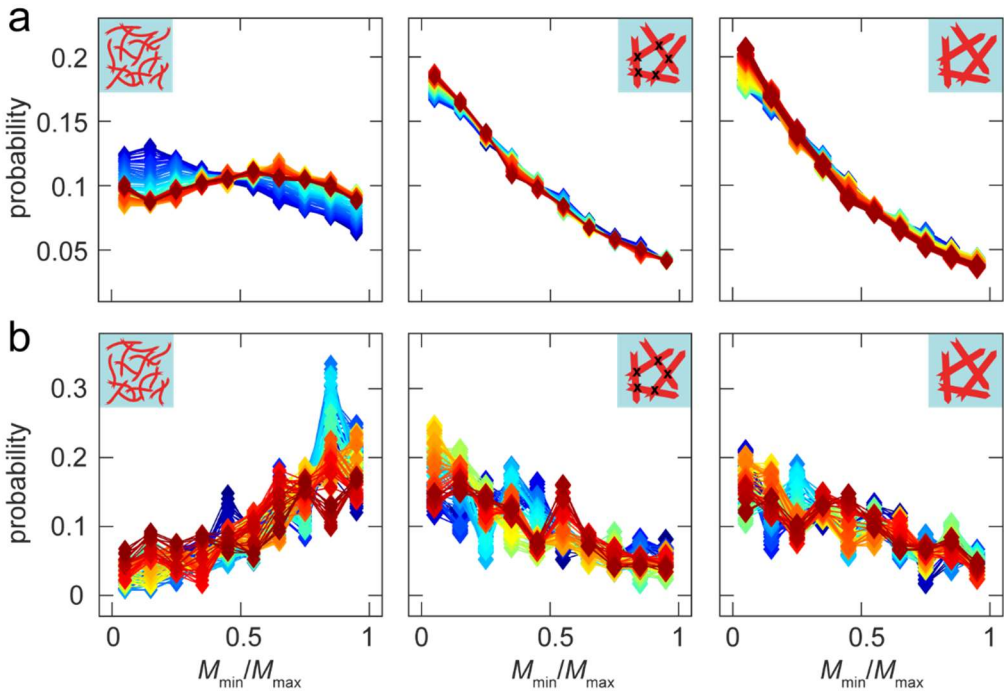

Figure 3.5 Networks have different contributions of biaxial and uniaxial deformations at varying length scales. (a) Distributions of M_{min}/M_{max} with s = 6 μm for network of semi-flexible filaments, cross-linked rigid bundles, and uncross-linked rigid bundles from left to right. (b) Distributions of M_{min}/M_{max} for same samples as (a) with s = 60 μm.

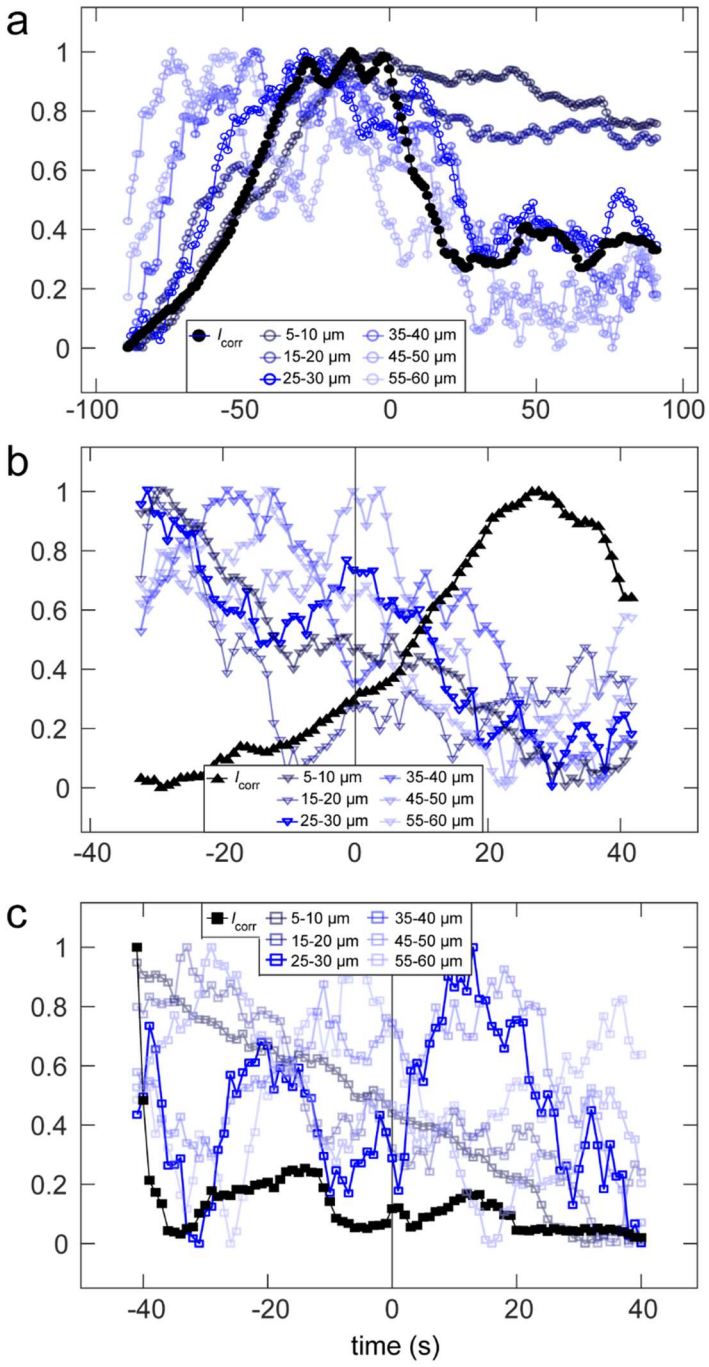

Figure 3.6 $P_{biaxial}$ at varying length scales has different trends over time for different networks. (a) $P_{biaxial}$ values at all varying length scales, s, (open blue circles, legend indicates value of s) initially increases and then decreases in network of semi-flexible filaments. At an intermediate value of s, the trend follows that of the correlation length, L_{corr} (filled black circles). (b) $P_{biaxial}$ at varying s (open blue triangles) decreases upon addition of myosin in network of cross-linked rigid bundles, while L_{corr} (filled black circles) increases. (c) $P_{biaxial}$ (open blue squares) at small s decreases after myosin addition in network of uncross-linked bundles but does not have a clear trend on longer length scales. Unlike the other two networks, L_{corr} decreases after myosin addition (filled black squares). For all curves, the values are shifted and scaled to range from 0 to 1.

positively correlated with l_{corr} and is optimized for a given length scale s (Methods, Fig. 3.6). In networks of semi-flexible filaments, $p_{biaxial}$ is positively correlated with l_{corr} during network contraction (Fig. 3.7a). In contrast, for the cross-linked rigid bundle networks, $p_{uniaxial}$ is strongly positively correlated with l_{corr} (Fig. 3.7b and Fig. 3.6b). Interestingly, there is a time lag from the maximal contraction (minimum divergence) to the maximum l_{corr} and $p_{uniaxial}$, which may arise from the higher sensitivity of the divergence measurement to biaxial contraction, as compared to uniaxial contraction. These data demonstrate that contractility can occur in networks composed of either semi-flexible or rigid filaments, consistent with previous reports of contractility in cross-

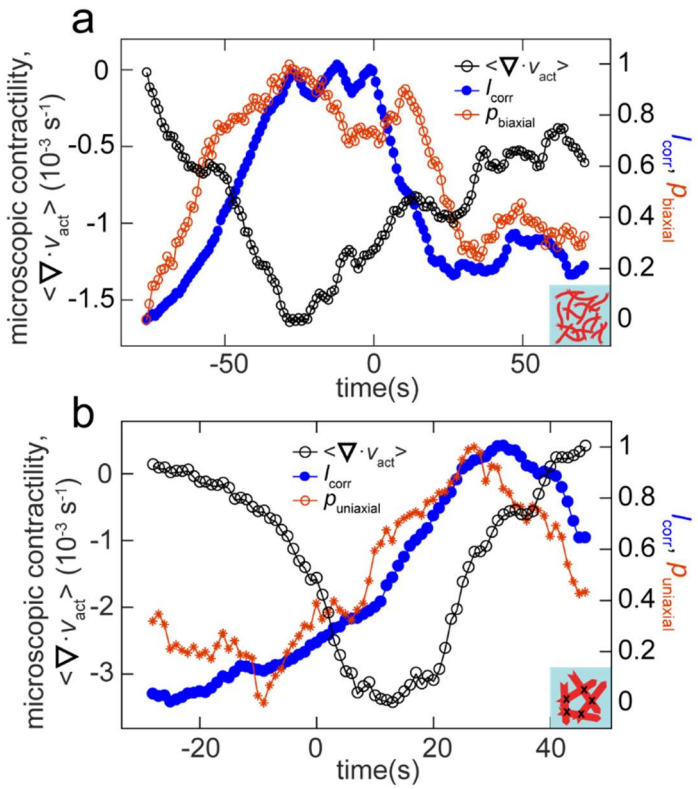

Figure 3.7 Activation of biaxial or uniaxial deformations in semi-flexible filament and rigid bundle networks respectively coincides with correlated motion and contractility. Plot of the divergence (open black cricles), correlation length and either biaxial probability (a) or uniaxial probability (b) as a function of time for single filaments (a) and cross-linked rigid bundles (b). The length scale chosen to calculate biaxial or uniaxial probability is determined to be the optimal one, as shown in Fig. S4 and is s = 25-30 μm in (a) and 55-60 μm in (b).

linked biopolymer networks of varying composition (53-56). Our analysis reveals significant differences, however, in the mesoscale shape changes induced within the two networks, with compliant networks supporting biaxial contraction and rigid networks supporting uniaxial deformations. Previously, we identified filament buckling as the microscopic mechanism underlying contractility in networks of semi-flexible actomyosin (55), an inherently biaxial deformation process. The mechanism underlying contractility in networks of rigid bundles is presumably different because buckling is suppressed by increased filament rigidity for a constant motor stress.

Uniaxial contraction arises from actomyosin sliding arrested by cross-linker accumulation

To elucidate the microscopic deformation modes underlying contraction in networks with varying filament rigidity, we use agent-based simulations (131). In brief, we model actin filaments as worm-like chains interacting with cross-linkers and motors represented as linear springs with two sites (heads) that can attach and detach to the filaments via a Monte Carlo procedure. When attached, motor heads walk toward filament barbed ends at a load-dependent speed. We use Langevin dynamics to evolve each structural component of the assembly in response to internal forces. When parameterized as detailed in (131), this model captures a variety of experimentally observed trends with reasonable quantitative accuracy. We implicitly model bundling, corresponding to experimental fascin-bundled actin, by varying the persistence length of the actin filament (L_p) between 25 and 250 μm. We explicity model cross-linking, corresponding to the experimental cross-linker filamin, by a spring with rest length 0.15 μm. Myosin miniflaments are

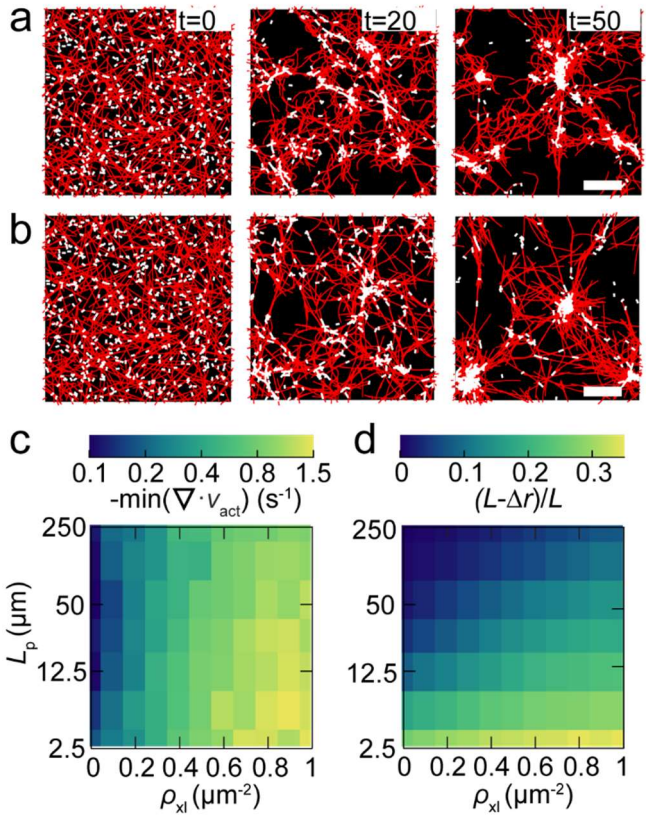

Figure 3.8 Simulations indicate cross-link dependent contractility over a wide range of filament stiffness. (a) and (b) Time series images in simulations for network with lower filament stiffness (L_p = 25 μm, (a)) and higher filament stiffness (L_p = 250 μm, (b)). Actin is shown in red and myosin is white. Scale bars are 10 μm. (c): Microscopic contractility at varying filament stiffness and cross-link density. This is measured by the minimum of the spatially averaged divergence of the actin velocity field weighted by the local actin density in the first 25 s of simulation. (d) Filament compression during the first 25 s of simulation as a function of stiffness and cross-link density.

modeled similarly, as springs with rest length 0.5 μm, unloaded speed v_0 = 1 μm/s, and stall force 10 pN.

We initially examine networks with filament rigidities similar to either actin filaments (persistence length, $L_p = 12.5\,\mu$m, Fig. 3.8a, Supplemental Movie S5) or fascin bundles (persistence length, L_p = 250 μm) and equal cross-linker densities ($\rho_{xl} = 1\,\mu\text{m}^{-2}$, Fig. 3.8b). Consistent with experiments, we observe that motors (white rectangles) move actin filaments and rearrange the filaments into asters. Both of these networks show comparable extents of contraction (Fig. 3.8c). Performing simulations over a range of filament rigidities (2.5 μm – 250 μm) and cross-linker densities (0 – 1 μm^{-2}) reveals that microscopic contractility is generally more sensitive to changes in cross-linker density than filament rigidity (Fig. 3.8c).

To explore the microscopic deformation modes underlying the regulation of contractility, we measure the filament deformation across these parameter values. One possible mechanism generating a net contractile deformation is filament buckling under local compressive forces (55, 65, 66). To quantify its extent, we measure the filament compression, $L - \Delta r/L$ where L is the filament contour length and Δr is the end-to-end distance. This measure is zero when filaments are perfectly straight ($\Delta r = L$) and greater than zero if they are bent. The amount of compression is highest in the cross-linked networks comprised of flexible filaments (Fig. 3.8d). Filament compression decreases as the cross-linker density is lowered and approaches zero as the filament rigidity increases (Fig. 3.8d). Comparison of Figs. 3.8c and 3.8d shows that there is a sizable region of parameter space over which contractility occurs in the absence of filament compression. At our highest filament rigidities (L_p > 100 μm), contraction occurs with $L - \Delta r/L$ less than 0.05 for

$\rho_{xl} < 0.5\ \mu\text{m}^{-2}$. Lower filament rigidities require lower cross-linker densities to maintain small filament deformations.

An alternate microscopic mechanism of contractility that we expect to be pronounced at higher rigidities is myosin-driven actin sliding (59, 61, 62). Actin sliding drives local contraction when a motor connected to two antiparallel filaments is closer to their pointed ends, and local extension when it is closer to their barbed ends (Fig. 3.9a). In the absence of symmetry-breaking mechanisms, this would result in no net force propagation as extensile and contractile deformation

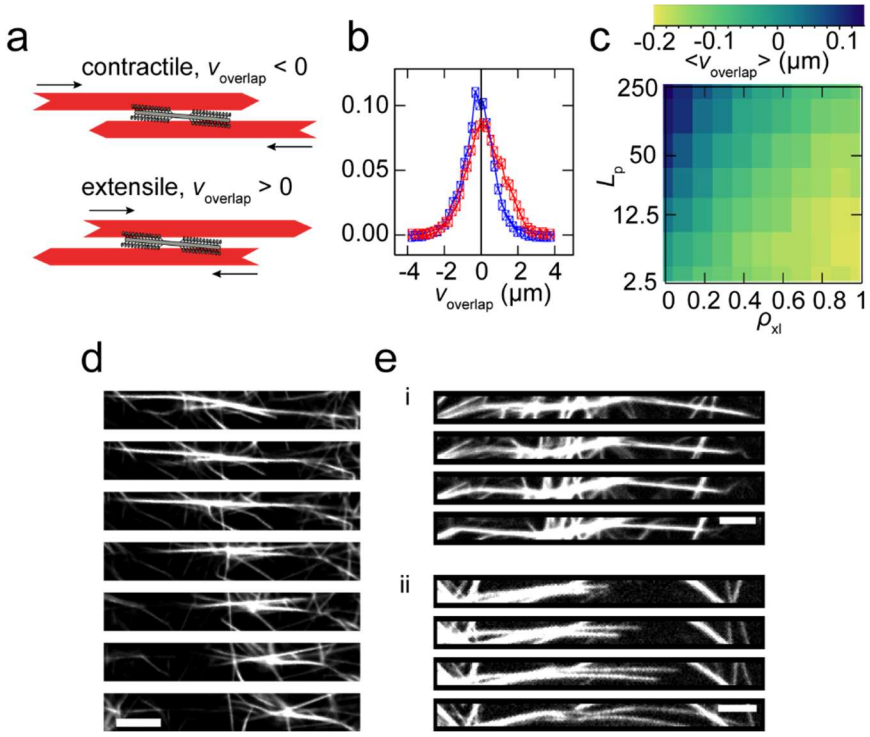

Figure 3.9 Uniaxial contractility is caused by arrested filament sliding. (a) A pair of antiparallel filaments are contractile if the myosin is near the pointed ends (top) and extensile is myosin is proximal to the barbed ends (bottom). (b) The distribution of $v_{overlap}$ is shifted to more extensile values for rigid (L_p = 250 μm) filaments without cross-linking (red squares) compared to the same filaments with ρ_{xl} = 1 μm^{-2} (blue squares). This distribution is from the first 10 s of simulation. (c) Average of $v_{overlap}$ over 25 s of simulation with varying filament rigidity and cross-link density. (d) In experiments with cross-linked rigid bundles, the bundles are observed to slide together and become arrested in the contracted state. The time delay between images from top to bottom is 1 s (e): In the absence of filamin, myosin drives both contractile (i) and extensile (ii) motions of rigid bundle pairs. The time delay between frames from top to bottom in both (i) and (ii) is 1 s Scale bars are 5 μm in (d) and (e).

ns would balance. However, when filaments overlap, there are more sites for cross-linkers to bind bivalently. This suppresses extensile motions that propagate force into the surrounding network (59). In the absence of cross-linkers, extensile motions can be favored by two mechanisms. First, for a uniform likelihood of myosin binding along the filament length, extensile antiparallel sliding will dominate (59, 60). Second, when the filaments reach the point of maximal overlap, they offer more available binding sites for motors to bivalently attach, which further increases extensile sliding (59, 60).

We examine the probability distribution of relative sliding velocity, v_{overlap}, in simulations of rigid (L_p = 250 μm) filaments both with ($\rho_{xl} = 1\,\mu\text{m}^{-2}$) and without cross-linkers. The distribution of overlap velocities shifts to negative values with the addition of cross-linkers (Fig. 3.9b). By examining the relative sliding velocity across all parameter values, we observe that the system is contractile ($\langle v_{overlap} \rangle < 0$) over most rigidities and cross-linker densities (Fig. 3.9c). However, at the lowest cross-linker densities and highest filament rigidities, we observe a regime where $\langle v_{overlap} \rangle > 0$, indicating that extensile motions dominate.

To seek evidence for extensile sliding in our experiment, we examined pairs of bundles undergoing relative sliding. Indeed, in the presence of cross-links between bundles (1:500 filamin:actin) we observe bundle pairs sliding relative to each other, increasing the overlap, and then stopping (Fig. 3.9d). In a network without cross-links between rigid bundles, we see both relative motion between bundles that increases their overlap (Fig. 3.9e(i)) and relative motion that extends bundles further apart (Fig. 3.9e(ii)). The latter is similar to extensile motions observed in

active liquid crystals of microtubules and kinesin (58), leading to the formation of asters (132, 133). Thus, our simulations and experiments of rigid filament suggests that cross-linker density can control the transition from contractile to extensile behaviors.

Motors drive aster formation within rigid bundles without cross-links via uniaxial, extensile forces

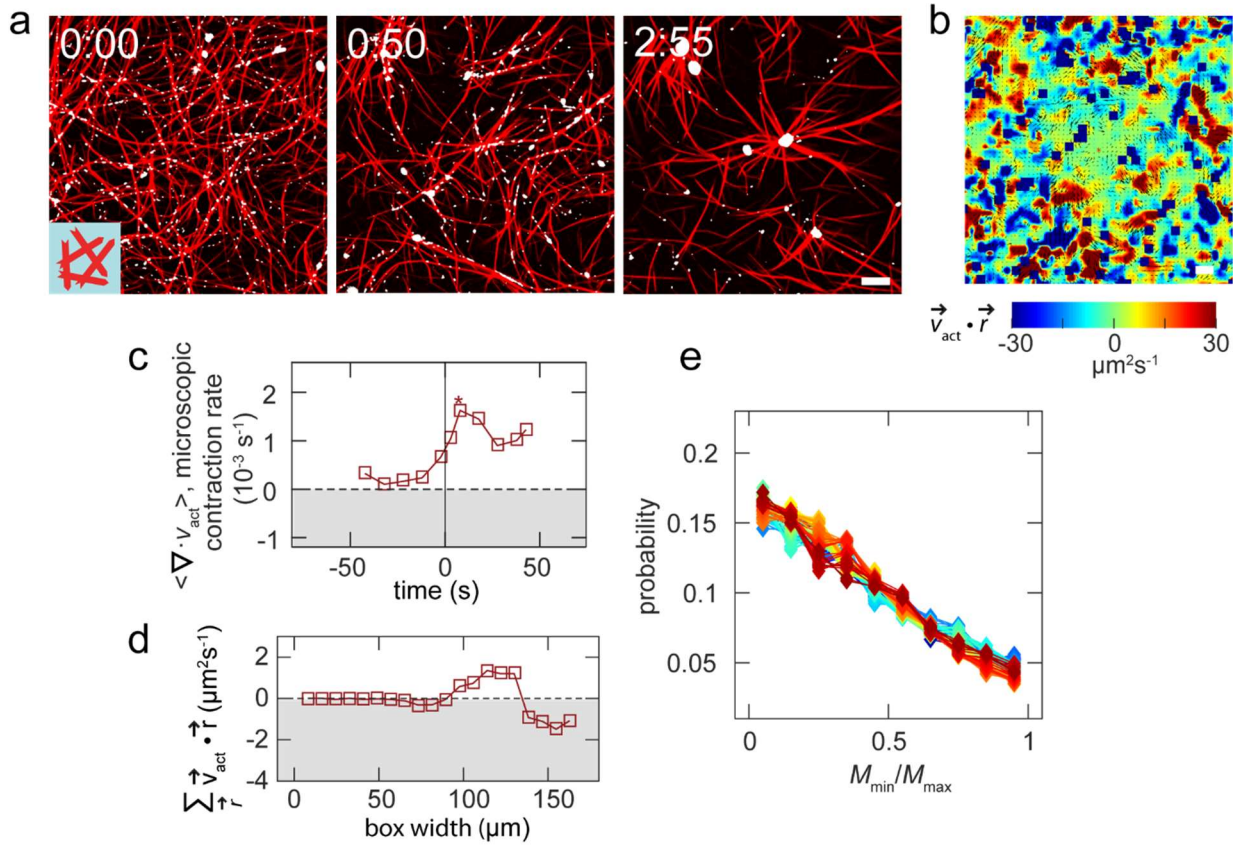

Figure 3.10 Myosin re-organizes rigid bundles lacking filamin cross-links via extensile uniaxial forces (a) Image sequence of fascin bundles without filamin. Actin is shown in red and myosin in white. (b) Values of $\vec{v}_{act} \cdot \vec{r}$ over a 150 μm x 150 μm square region. (c) The divergence of $\vec{v}_{act}$ is non-contractile over the course of network rearrangement. (d) The contractile moment, $\langle \sum_{\vec{r}} \vec{v}_{act} \cdot \vec{r} \rangle$, calculated over a 30 s interval after the maximum divergence in (c). (e) Distribution of M_{min}/M_{max}, s = 20 μm, indicates that deformations are predominantly uniaxial.

To understand the consequences of the microscopic extensile deformations described above, we study the myosin-driven reorganization of rigid actin bundles that lack filamin cross-linkers but are sufficiently dense to have numerous overlaps such that myosin motors can slide and rearrange bundles to eventually form asters (Fig. 3.10a). Asters are comprised of a dense myosin cluster with polarity sorted actin bundles emanating from the center, similar to those previously described (Figs. 3.3 and 3.10a). The spatial map of the moment of the velocity field reveals small contractile and extensile regions that are interspersed (Fig. 3.10b) and the velocity-velocity correlation length is short (Fig. 3.11). Consistent with simulations (Fig. 3.9c), the divergence of the velocity field indicates net extensile deformation (Fig. 3.10c), and the contractile moment is weakly positive at ~100 μm (Fig. 3.10d). The minimum divergence of the velocity field is weakly negative if the PIV vectors are calculated at sufficiently large time delays and length scales, but the divergence values are always less negative than in the other two networks (Fig. 3.12). Consistent with motions dominated by actomyosin sliding, deformations are predominantly

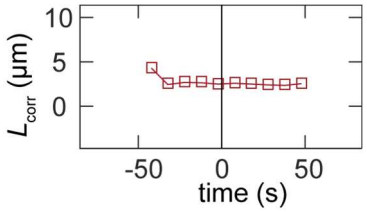

Figure 3.11 Data for network of rigid bundles without cross-links. Unscaled L_{corr} as a function of time.

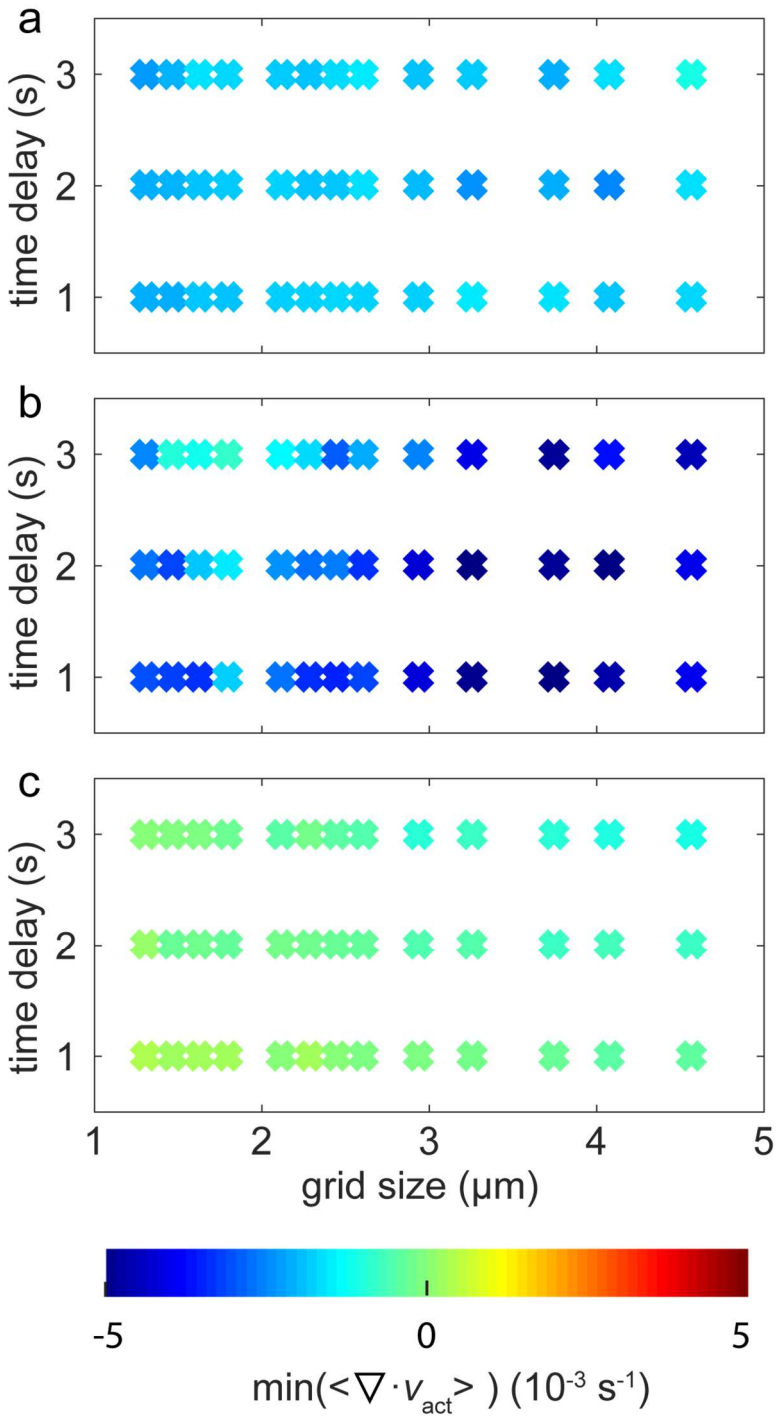

Figure 3.12 Minimum of $<\nabla \cdot \vec{v}_{act}>$ for PIV vectors calculated with varying time delay and length scale. The minimum of the spatially averaged divergence is indicated by the color scale for semi-flexible filaments (a), cross-linked rigid bundles (b), and rigid bundles without cross-links (c).

uniaxial (Fig. 3.10e). Thus, actin sliding is responsible for short-range extensile, uniaxial deformations that drive local rearrangement of actin bundles into polarity-sorted asters.

3.4 Discussion

Our results reveal three phases of deformation characterized by their anisotropy, length scale, and contractility. These can be controlled by modifying filament rigidity and connectivity in active biopolymer networks (Fig. 3.13). Moreover, we then demonstrate each phase is consistent with a unique microscopic deformation mode. In the presence of cross-linkers, we find that filament rigidity drives a transition between buckling-dominated and sliding-dominated contraction and, consequently, a transition between biaxial and uniaxial deformations. Such control over the shape of the deformations could be used to sculpt active materials both *in vitro* and *in vivo*. For rigid filaments, we find that increased cross-linking drives a transition from extensile to contractile deformation. While the role of cross-linking has been well described in terms of controlling force transmission (53, 54, 67, 71, 111), our work suggests that it also plays an important role in controlling the direction of the deformation, namely changing it from extensile to contractile. This result unifies previous observations of both extensile and contractile behaviors in active microtubule systems (57-60, 113, 114), suggesting that network connectivity is a significant factor in determining which behavior predominates. In future work, it will be interesting to explore the transitions between other microscopic deformation modes in active motor-filament systems and see how these are controlled by local structure or composition (e.g., filament orientation or polarity organization).

The myosin-driven remodeling of actin networks with varied connectivity and rigidity results in polarity-sorted asters of actin with high myosin densities at their centers, consistent with

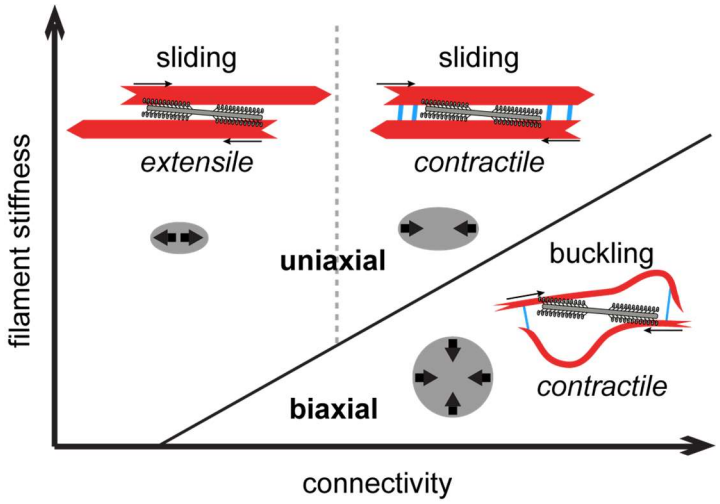

Figure 3.13 State space on force generation in active matter comprised of motors and filaments. Starting from the top left of the diagram, the three states we observe are extensile sliding, contractile sliding, and contractile buckling. The shape of the boundaries between these mechanisms are based on the simulation phase spaces in Fig. 3.8c and Fig. 3.9d. The mechanisms can be identified by the characteristic anisotropy of the transmitted forces, which is predominantly uniaxial for sliding and biaxial for buckling.

previous experiments reporting cluster formation (53-56, 68, 71, 113, 114, 132-136). Many of these studies have equated cluster formation with contraction, and associated theoretical models have assumed that motors produce contractile force dipoles (137). However, our analysis shows that the microscopic driving forces and deformation modes to construct asters can include both isotropic and anisotropic contractility as well as anisotropic extension. While these generally result in differences in the actin distribution in the final structure (Fig. 3.3), our results show that different microscopic mechanics can result in similar final organizations. This underscores the importance of characterizing the dynamical rearrangements during active processes rather than relying on final structures alone to elucidate physical mechanisms.

Our work has implications for assessing and understanding the underlying physical mechanisms of force propagation in a variety of active biopolymer systems. Motor-filament arrays are a common motif in the actin and microtubule cytoskeletons during processes, including cell migration, cell division, intracellular transport, and formation of the mitotic spindle. Beyond the

cytoskeleton, intranuclear molecular motors can drive correlated motion of chromatin (138), and forces produced by whole bacterial or mammalian cells can drive motions such as biofilm contraction or growth (139, 140) or alignment and organization of filamentous extracellular matrices (141-143). The physical properties of deformations that occur during these processes and the mechanisms at the level of biopolymer deformation or translocation have not been explored. Investigations of this nature will reveal which features of active matter dynamics are fundamental across these highly diverse systems and which features are regulated by particular biopolymer and motor network properties.

Chapter 4 Conclusions

In conclusion, this thesis examines the effect of actin network mechanical properties on force generation and transmission in actomyosin networks. We first map different regimes of force generation by myosin II filaments using simulations in Chapter 2. In the presence of catch-bond kinetics, we find a steep transition in the affinity of a myosin filament for actin at a threshold stiffness an elastic load resisting actin sliding. The stiffness value at which this occurs is tunable depending on isoform-specific myosin filament properties. Below this threshold, myosin filaments have a very low affinity for actin and build small, transient forces on the elastic load. Above the threshold, myosin either builds a large, stable force or is alternatively sufficiently slow that it could act as a high-affinity cross-linker rather than an effective generator of force, again depending on the properties of the isoform. This clarifies the role of stiffness and the myosin catch bond, and suggests that coarse-grained representation of myosin activity as force dipoles should consider different values of two critical timescales: the force duration, and buildup time.

An example of coarse-grained models that could be informed by this work involve understanding how cells can sense environmental stiffness—a process that is believed to be important for stem-cell differentiation, regulation of cell shape, and the direction of cell migration (82). One theoretical model has indicated that polarization of the forces generated in the cytoskeleton, which could be important in allowing cells to adopt or maintain a particular morphology during differentiation, occurs optimally at an intermediate stiffness based on assuming a phenomenological, cell-type specific polarization parameter (144). The assumed polarization parameter gave rise to anisotropy in the force dipoles exerted in the cytoskeleton by effectively enforcing that higher cytoskeletal forces were exerted in the direction of higher traction

stresses occurring due to adhesion of the cell to a substrate. Provided that a cell's aspect ratio was greater than one, a higher anisotropy in these traction stresses occurred at the optimal stiffness. This caused the observed sensitivity of cytoskeletal force polarization to stiffness. Presumably, the physical explanation of polarizability in the cellular forces could either involve reorientation of myosin filaments or other generators of force, or changes in their force output depending on their existing orientation. In this reference, the orientation of stress fibers—thick bundles of actin and myosin found in some cell types—was used as evidence of force polarization in experiments.

However, whether assembling or reorienting stress fibers in response to increases or gradients in the local stress is truly the microscopic mechanism for adjustment of a cell's force output in response to environmental stiffness is unclear. For example, a theoretical model that neglected differences in stress fiber formation has successfully described a cell's strain energy output on varying substrates (145). Understanding the microscopic requirements for stiffness sensing at the level of the cytoskeletal networks and motors is still an unanswered question.

These details matter if we are to understand which physical and biochemical cytoskeletal network conditions will allow phenomena such as stiffness sensing to occur. For example, if force dipole reorientation is the necessary regulatory step, then an actin network that allows myosin or stress fibers sufficient mobility to reorient may permit stiffness sensing, while a network that is highly crowded might suppress it. Alternatively, molecular machinery that preferentially polymerizes myosin filaments or actin filaments along the direction of highest local stress could be necessary. However, if, as our work suggests, a strong dependence of force output on local stress or stiffness occurs due to the inherent mechanochemical properties of the myosin filaments, then polarized orientation would not be necessary to produce a polarized force. An important next step to test these possibilities is to construct network-level models with a more accurate

representation of the myosin forces and to determine whether such models are also capable of reproducing existing experimental data of cellular stiffness sensing. Further experiments and modeling will be necessary to differentiate which model or models are the most appropriate explanations of the observed data.

In the second project of this thesis, we find different regimes with characteristic spatial patterns of force propagation using a combination of experiments, image analysis, and simulation in Chapter 3. Networks of rigid filaments produce highly elongated, uniaxial deformations that can span over tens of microns while semi-flexible actin filaments produce biaxial deformations on similar length scales. Simulations indicate that the underlying force dipoles being transmitted in these networks arise from relative filament sliding and filament buckling respectively. Furthermore, the deformations of rigid filament networks may be tuned from extensile to contractile with the addition of cross-linkers between filaments. This occurs because the attachment of cross-linkers to sliding rigid filaments in the fully contracted state effectively increases the stiffness that the motors must work against to slide them further, and extensile sliding is arrested.

The observation of varying deformation shape due to filament buckling versus filament sliding is a first step toward directly detecting the microscopic deformation mechanism in a variety of active networks. In simplified *in vitro* systems, labeling of individual filaments can allow for direct observation of mechanisms such as filament buckling (55). However, other previous studies have relied on comparison between theoretical models and experimental measurements of generated force (146), contraction velocity (67, 146), or extent of contraction (67) to demonstrate that polymer sliding or buckling are feasible mechanisms under certain conditions. Our results do not replace theoretical modeling efforts, but rather indicate that deformation anisotropy may

provide valuable quantitative evidence for or against such explanations for the observed network behavior. Again, understanding the detailed mechanism is important because the physical and biochemical properties of a cytoskeletal network that a cell must regulate to make a specific deformation possible will differ depending on which mode(s) of deformation are used.

More generally, there are, to our knowledge, no previous examples of deformation anisotropy analysis having been conducted in active biopolymer networks. Anisotropy analysis has typically been used to study the traction forces exerted on a substrate by individual cells (147, 148), two dividing cells (149), or cell monolayers moving collectively (150). It will be interesting to see which deformations, defined by their anisotropy and length scale, are activated or deactivated during a particular intracellular process or during changes in density of particular motor proteins. This will clarify the physical requirements for successful completion of a physiological process involving network deformation. For example, it is unknown whether or not cytokinesis requires deformations that are sufficiently anisotropic and parallel to the division plane of two cells. It is also unknown how long-range or how anisotropic contractions that produce retraction of the cell rear during migration must be for the cell to successfully navigate crowded environments. Many other examples of deformation processes involving the cytoskeleton and other biopolymer networks could be similarly informed by such analysis.

Together, this thesis informs future studies on how mechanical properties of biopolymer networks regulate the activity of internal motor proteins as well as the type of deformations the networks undergo. This is an important step toward a more detailed understanding of physiological processes than can be obtained from coarse-grained theoretical models alone. Future studies will continue to reveal the microscopic mechanisms behind observations of cell motion, proliferation, shape change, and sensitivity to the environment.

References

1. Gautel M & Djinović-Carugo K (2016) The sarcomeric cytoskeleton: from molecules to motion. *The Journal of Experimental Biology* 219(2):135.
2. Fededa JP & Gerlich DW (2012) Molecular control of animal cell cytokinesis. *Nat Cell Biol* 14(5):440-447.
3. Munro E, Nance J, & Priess JR (2004) Cortical flows powered by asymmetrical contraction transport PAR proteins to establish and maintain anterior-posterior polarity in the early C-elegans embryo. *Developmental Cell* 7(3):413-424.
4. Blanchoin L, Boujemaa-Paterski R, Sykes C, & Plastino J (2014) Actin Dynamics, Architecture, and Mechanics in Cell Motility. *Physiological Reviews* 94(1):235-263.
5. Murrell M, Oakes PW, Lenz M, & Gardel ML (2015) Forcing cells into shape: the mechanics of actomyosin contractility. *Nat Rev Mol Cell Biol* 16(8):486-498.
6. Hill AV (1938) The Heat of Shortening and the Dynamic Constants of Muscle. *Proceedings of the Royal Society of London. Series B - Biological Sciences* 126(843):136.
7. Huxley AF (1957) Muscle structure and theories of contraction. *Prog. Biophys. Biophys. Chem.* 7:255-318.
8. Hanson J & Huxley HE (1953) Structural Basis of the Cross-Striations in Muscle. *Nature* 172(4377):530-532.
9. Huxley HE (1953) Electron microscope studies of the organisation of the filaments in striated muscle. *Biochimica et Biophysica Acta* 12(1):387-394.
10. Huxley H & Hanson J (1954) Changes in the Cross-Striations of Muscle during Contraction and Stretch and their Structural Interpretation. *Nature* 173(4412):973-976.
11. Huxley AF & Niedergerke R (1954) Structural Changes in Muscle During Contraction: Interference Microscopy of Living Muscle Fibres. *Nature* 173(4412):971-973.
12. Huxley HE (1969) The Mechanism of Muscular Contraction. *Science* 164(3886):1356.
13. Sheetz MP & Spudich JA (1983) Movement of Myosin-Coated Fluorescent Beads on Actin Cables Invitro. *Nature* 303(5912):31-35.
14. Kron SJ & Spudich JA (1986) Fluorescent Actin-Filaments Move on Myosin Fixed to a Glass-Surface. *Proceedings of the National Academy of Sciences of the United States of America* 83(17):6272-6276.
15. Oiwa K, Chaen S, Kamitsubo E, Shimmen T, & Sugi H (1990) Steady-state force-velocity relation in the ATP-dependent sliding movement of myosin-coated beads on actin cables in vitro studied with a centrifuge microscope. *Proceedings of the National Academy of Sciences* 87(20):7893-7897.
16. Debold EP, Patlak JB, & Warshaw DM (2005) Slip sliding away: Load-dependence of velocity generated by skeletal muscle myosin molecules in the laser trap. *Biophysical Journal* 89(5):L34-L36.
17. Tregear RT & Squire JM (1973) Myosin content and filament structure in smooth and striated muscle. *Journal of Molecular Biology* 77(2):279-290.
18. Marchetti MC*, et al.* (Hydrodynamics of soft active matter. *Reviews of Modern Physics* 85(3):1143.
19. Toner J & Tu Y (1995) Long-Range Order in a Two-Dimensional Dynamical XY Model: How Birds Fly Together. *Physical Review Letters* 75(23):4326-4329.

20. Vicsek T, Czirók A, Ben-Jacob E, Cohen I, & Shochet O (1995) Novel Type of Phase Transition in a System of Self-Driven Particles. *Physical Review Letters* 75(6):1226-1229.
21. Carlsson AE (2006) Contractile stress generation by actomyosin gels. *Physical Review E* 74(5):051912.
22. Safran SA, Nicolas A, & Schwarz US (2005) Elastic Interactions of Biological Cells. *Mechanics of the 21st Century: Proceedings of the 21st International Congress of Theoretical and Applied Mechanics, Warsaw, Poland, 15–21 August 2004*, eds Gutkowski W & Kowalewski TA (Springer Netherlands, Dordrecht), pp 329-342.
23. Baskaran A & Marchetti MC (2009) Statistical mechanics and hydrodynamics of bacterial suspensions. *Proceedings of the National Academy of Sciences* 106(37):15567-15572.
24. Rosenfeld SS, Xing J, Chen LQ, & Sweeney HL (2003) Myosin IIb is unconventionally conventional. *J Biol Chem* 278(30):27449-27455.
25. Norstrom MF, Smithback PA, & Rock RS (2010) Unconventional Processive Mechanics of Non-muscle Myosin IIB. *Journal of Biological Chemistry* 285(34):26326-26334.
26. Wang F*, et al.* (2003) Kinetic mechanism of non-muscle myosin IIB: functional adaptations for tension generation and maintenance. *J. Biol. Chem.* 278:27439-27448.
27. Kovacs M, Wang F, Hu A, Zhang Y, & Sellers JR (2003) Functional divergence of human cytoplasmic myosin II: kinetic characterization of the non-muscle IIA isoform. *J. Biol. Chem.* 278(40):38132-38140.
28. Harris DE & Warshaw DM (1993) Smooth and skeletal-muscle myosin both exhibit low duty cycles at zero load in-vitro. *J. Biol. Chem.* 268(20):14764-14768.
29. Nagy A*, et al.* (2013) Kinetic characterization of nonmuscle myosin IIb at the single molecule level. *J Biol Chem* 288(1):709-722.
30. Mizuno D, Tardin C, Schmidt CF, & MacKintosh FC (2007) Nonequilibrium Mechanics of Active Cytoskeletal Networks. *Science* 315(5810):370.
31. Lau AWC, Hoffman BD, Davies A, Crocker JC, & Lubensky TC (2003) Microrheology, Stress Fluctuations, and Active Behavior of Living Cells. *Physical Review Letters* 91(19):198101.
32. Hoffman BD, Massiera G, Van Citters KM, & Crocker JC (2006) The consensus mechanics of cultured mammalian cells. *Proceedings of the National Academy of Sciences* 103(27):10259-10264.
33. Lin CH, Espreafico EM, Mooseker MS, & Forscher P (1996) Myosin Drives Retrograde F-Actin Flow in Neuronal Growth Cones. *Neuron* 16(4):769-782.
34. Sobieszek A (1972) Cross-bridges on self-assembled smooth muscle myosin filaments. *J. Mol. Biol.* 70(3):741-744.
35. Tonino P, Simon M, & Craig R (2002) Mass determination of native smooth muscle myosin filaments by scanning transmission electron microscopy. *J. Mol. Biol.* 318(4):999-1007.
36. Niederman R & Pollard TD (1975) Human platelet myosin. II. *In vitro* assembly and structure of myosin filaments. *J. Cell Biol.* 67(1):72-92.
37. Pollard TD (1982) Structure and polymerization of acanthamoeba myosin-II filaments. *J. Cell Biol.* 95(3):816-825.
38. Finer JT, Simmons RM, & Spudich JA (1994) Single myosin molecule mechanics: piconewton forces and nanometre steps. *Nature* 368(6467):113-119.
39. Tyska MJ*, et al.* (1999) Two heads of myosin are better than one for generating force and motion. *Proceedings of the National Academy of Sciences* 96(8):4402-4407.

40. Miyata H, Yasuda R, & Kinosita K (1996) Strength and lifetime of the bond between actin and skeletal muscle alpha-actinin studied with an optical trapping technique. *Biochimica Et Biophysica Acta-General Subjects* 1290(1):83-88.
41. Wachsstock DH, Schwarz WH, & Pollard TD (1994) Cross-linker Dynamics Determine the Mechanical Properties of Actin Gels. *Biophysical Journal* 66(3):801-809.
42. Theriot JA & Mitchison TJ (1991) Actin microfilament dynamics in locomoting cells. *Nature* 352(6331):126-131.
43. Harris DE & Warshaw DM (1993) Smooth and skeletal muscle myosin both exhibit low duty cycles at zero load in vitro. *J Biol Chem* 268(20):14764-14768.
44. Cuda G, Pate E, Cooke R, & Sellers JR (1997) In vitro actin filament sliding velocities produced by mixtures of different types of myosin. *Biophys J* 72(4):1767-1779.
45. Umemoto S & Sellers JR (1990) Characterization of in vitro motility assays using smooth muscle and cytoplasmic myosins. *Journal of Biological Chemistry* 265(25):14864-14869.
46. Veigel C, Molloy JE, Schmitz S, & Kendrick-Jones J (2003) Load-dependent kinetics of force production by smooth muscle myosin measured with optical tweezers. *Nat. Cell Biol.* 5(11):980-986.
47. Guo B & Guilford WH (2006) Mechanics of actomyosin bonds in different nucleotide states are tuned to muscle contraction. *Proc. Natl. Acad. Sci. USA* 103(26):9844-9849.
48. Kovacs M, Thirumurugan K, Knight PJ, & Sellers JR (2007) Load-dependent mechanism of nonmuscle myosin 2. *Proc Natl Acad Sci U S A* 104(24):9994-9999.
49. Duke TA (1999) Molecular model of muscle contraction. *Proc. Natl. Acad. Sci. USA* 96:2770-2775.
50. Mitrossilis D*, et al.* (2009) Single-cell response to stiffness exhibits muscle-like behavior. *Proc. Natl. Acad. Sci. USA* 106:18243-18248.
51. Borau C, Kim T, Bidone T, Garcia-Aznar JM, & Kamm RD (2012) Dynamic mechanisms of cell rigidity sensing: insights from a computational model of actomyosin networks. *PloS one* 7(11):e49174.
52. Walcott S & Sun SX (2010) A mechanical model of actin stress fiber formation and substrate elasticity sensing in adherent cells. *Proc. Natl. Acad. Sci. USA* 107(17):7757-7762.
53. Janson LW, Kolega J, & Taylor DL (1991) Modulation of Contraction by Gelation Solation in a Reconstituted Motile Model. *Journal of Cell Biology* 114(5):1005-1015.
54. Alvarado J, Sheinman M, Sharma A, MacKintosh FC, & Koenderink GH (2013) Molecular motors robustly drive active gels to a critically connected state. *Nature Physics* 9(9):591-597.
55. Murrell MP & Gardel ML (2012) F-actin buckling coordinates contractility and severing in a biomimetic actomyosin cortex. *Proceedings of the National Academy of Sciences of the United States of America* 109(51):20820-20825.
56. Koehler S & Bausch AR (2012) Contraction Mechanisms in Composite Active Actin Networks. *Plos One* 7(7).
57. Sanchez T, Chen DT, DeCamp SJ, Heymann M, & Dogic Z (2012) Spontaneous motion in hierarchically assembled active matter. *Nature* 491(7424):431-434.
58. Henkin G, DeCamp SJ, Chen DT, Sanchez T, & Dogic Z (2014) Tunable dynamics of microtubule-based active isotropic gels. *Philos Trans A Math Phys Eng Sci* 372(2029).
59. Blackwell R*, et al.* (2016) Microscopic origins of anisotropic active stress in motor-driven nematic liquid crystals. *Soft Matter* 12(10):2676-2687.

60. Gao T, Blackwell R, Glaser M, Betterton M, & Shelley M (2015) Multiscale Polar Theory of Microtubule and Motor-Protein Assemblies. *Physical Review Letters* 114(4).
61. Liverpool TB & Marchetti MC (2005) Bridging the microscopic and the hydrodynamic in active filament solutions. *EPL (Europhysics Letters)* 69(5):846.
62. Kruse K & Julicher F (2000) Actively contracting bundles of polar filaments. *Physical Review Letters* 85(8):1778-1781.
63. Kojima H, Ishijima A, & Yanagida T (1994) Direct measurement of stiffness of single actin filaments with and without tropomyosin by in vitro nanomanipulation. *Proc Natl Acad Sci U S A* 91(26):12962-12966.
64. Gittes F, Mickey B, Nettleton J, & Howard J (1993) Flexural Rigidity of Microtubules and Actin-Filaments Measured from Thermal Fluctuations in Shape. *Journal of Cell Biology* 120(4):923-934.
65. Liverpool TB, Marchetti MC, Joanny JF, & Prost J (2009) Mechanical response of active gels. *EPL (Europhysics Letters)* 85(1):18007.
66. Lenz M, Thoresen T, Gardel ML, & Dinner AR (2012) Contractile Units in Disordered Actomyosin Bundles Arise from F-Actin Buckling. *Physical Review Letters* 108(23).
67. Ennomani H*, et al.* (2016) Architecture and Connectivity Govern Actin Network Contractility. *Curr Biol* 26(5):616-626.
68. Vogel SK, Petrasek Z, Heinemann F, & Schwille P (2013) Myosin motors fragment and compact membrane-bound actin filaments. *Elife* 2.
69. Dasanayake NL, Michalski PJ, & Carlsson AE (2011) General Mechanism of Actomyosin Contractility. *Physical Review Letters* 107(11).
70. Lenz M (2014) Geometrical Origins of Contractility in Disordered Actomyosin Networks. *Physical Review X* 4(4):041002.
71. Bendix PM*, et al.* (2008) A quantitative analysis of contractility in active cytoskeletal protein networks. *Biophysical Journal* 94(8):3126-3136.
72. Stam S, Alberts J, Gardel ML, & Munro E (2015) Isoforms Confer Characteristic Force Generation and Mechanosensation by Myosin II Filaments. *Biophys J* 108(8):1997-2006.
73. Stam S*, et al.* (2017) Filament Rigidity And Connectivity Tune The Deformation Modes Of Active Biopolymer Networks. *bioRxiv*.
74. Gordon AM, Homsher E, & Regnier M (2000) Regulation of contraction in striated muscle. *Physiol. Rev.* 80(2):853-924.
75. Lofgren M, Malmqvist U, & Arner A (2001) Substrate and product dependence of force and shortening in fast and slow smooth muscle. *J. Gen. Physiol.* 117(5):407-418.
76. Vicente-Manzanares M, Ma X, Adelstein RS, & Horwitz AR (2009) Non-muscle myosin II takes centre stage in cell adhesion and migration. *Nat. Rev. Mol. Cell Biol.* 10(11):778-790.
77. Gardel ML, Schneider IC, Aratyn-Schaus Y, & Waterman CM (2010) Mechanical integration of actin and adhesion dynamics in cell migration. *Annu. Rev. Cell Dev. Biol.* 26:315-333.
78. Matsumura F (2005) Regulation of myosin II during cytokinesis in higher eukaryotes. *Trends Cell Biol* 15(7):371-377.
79. Carvalho A, Desai A, & Oegema K (2009) Structural memory in the contractile ring makes the duration of cytokinesis independent of cell size. *Cell* 137(5):926-937.
80. Lecuit T, Lenne PF, & Munro E (2011) Force generation, transmission, and integration during cell and tissue morphogenesis. *Annu. Rev. Cell Dev. Biol.* 27:157-184.

81. Munro E & Bowerman B (2009) Cellular symmetry breaking during Caenorhabditis elegans development. *Cold Spring Harb. Perspect. Biol.* 1(4):a003400.
82. Hoffman BD, Grashoff C, & Schwartz MA (2011) Dynamic molecular processes mediate cellular mechanotransduction. *Nature* 475(7356):316-323.
83. Discher DE, Janmey P, & Wang YL (2005) Tissue cells feel and respond to the stiffness of their substrate. *Science* 310(5751):1139-1143.
84. Spudich JA (2001) The myosin swinging cross-bridge model. *Nat. Rev. Mol. Cell Biol.* 2(5):387-392.
85. Hill TL (1974) Theoretical formalism for the sliding filament model of contraction of striated muscle. Part I. *Prog. Biophys. Mol. Biol.* 28:267-340.
86. Piazzesi G & Lombardi V (1995) A cross-bridge model that Is able to explain mechanical and energetic properties of shortening muscle. *Biophys. J.* 68(5):1966-1979.
87. Eisenberg E, Hill TL, & Chen Y (1980) Cross-bridge model of muscle-contraction - quantitative-analysis. *Biophys. J.* 29(2):195-227.
88. Pate E & Cooke R (1989) A Model of crossbridge action - the effects of ATP, ADP and Pi. *J. Mus. Res. Cell Motil.* 10(3):181-196.
89. Mansson A (2010) Actomyosin-ADP states, interhead cooperativity, and the force-velocity relation of skeletal muscle. *Biophys. J.* 98(7):1237-1246.
90. Lacker HM & Peskin CS (1986) A mathematical method for unique determination of cross-bridge properties from steady-state mechanical and energetic experiments on macroscopic muscle. *Some Mathematical Questions in Biology--Muscle Physiology*, ed Miura R (American Mathematical Society, Providence, RI), Vol 16, pp 121-153.
91. Walcott S, Warshaw DM, & Debold EP (2012) Mechanical coupling between myosin molecules causes differences between ensemble and single-molecule measurements. *Biophys. J.* 103(3):501-510.
92. Erdmann T, Albert PJ, & Schwarz US (2013) Stochastic dynamics of small ensembles of non-processive molecular motors: the parallel cluster model. *J. Chem. Phys.* 139(17):175104.
93. Erdmann T & Schwarz US (2012) Stochastic force generation by small ensembles of myosin II motors. *Phys. Rev. Lett.* 108(18):188101.
94. Hilbert L, Cumarasamy S, Zitouni NB, Mackey MC, & Lauzon AM (2013) The kinetics of mechanically coupled myosins exhibit group size-dependent regimes. *Biophys. J.* 105(6):1466-1474.
95. Marston SB & Taylor EW (1980) Comparison of the myosin and actomyosin ATPase mechanisms of the four types of vertebrate muscles. *J. Mol. Biol.* 139:573-600.
96. Cremo CR & Geeves MA (1998) Interaction of actin and ADP with the head domain of smooth muscle myosin: Implications for strain-dependent ADP release in smooth muscle. *Biochemistry* 37(7):1969-1978.
97. Steffen W, Smith D, Simmons R, & Sleep J (2001) Mapping the actin filament with myosin. *Proceedings of the National Academy of Sciences of the United States of America* 98(26):14949-14954.
98. Gillespie DT (1976) A general method for numerically solving the stochastic time evolution of coupled chemical reactions. *J. Comp. Phys.* 22:403-434.
99. Trybus KM & Taylor EW (1982) Transient kinetics of ADP and AMP-PNP binding to subfragment 1 and actosubfragment 1. *Biochemistry* 21(6):1284-1294.

100. White HD, Belknap B, & Webb MR (1997) Kinetics of nucleoside triphosphate cleavage and phosphate release steps by associated rabbit skeletal actomyosin, measured using a novel fluorescent probe for phosphate. *Biochemistry* 36(39):11828-11836.
101. Skubiszak L & Kowalczyk L (2002) Myosin molecule packing within the vertebrate-skeletal muscle thick filaments. A complete bipolar model. *Acta Biochim. Pol.* 49(4):829-840.
102. Umemoto S & Sellers JR (1990) Characterization of in vitro motility assay using smooth muscle and cytoplasmic myosins. *J. Biol. Chem.* 265:14864-14869.
103. Cuda G, Pate E, Cooke R, & Sellers JR (1997) In vitro actin filament sliding velocities produced by mixtures of different types of myosin. *Biophys. J.* 72:1767-1779.
104. Uyeda TQP, Kron SJ, & Spudich JA (1990) Myosin step size: estimation from slow sliding movement of actin over low densities of heavy meromyosin. *J. Mol. Biol.* 214(3):699-710.
105. Beach J*, et al.* (2014) Nonmuscle Myosin II Isoforms Coassemble in Living Cells. *Curr. Biol.* 24(10):1160-1166.
106. Wachsstock DH, Schwarz WH, & Pollard TD (1994) Cross-linker dynamics determine the mechanical-properties of actin gels. *Biophys. J.* 66(3):801-809.
107. Miyata H, Yasuda R, & Kinosita K (1996) Strength and lifetime of the bond between actin and skeletal muscle alpha-actinin studied with an optical trapping technique. *Biochim. Biophys. Acta-Gen. Subjects* 1290(1):83-88.
108. Gardel ML*, et al.* (2004) Elastic behavior of cross-linked and bundled actin networks. *Science* 304(5675):1301-1305.
109. Yuval J & Safran SA (2013) Dynamics of elastic interactions in soft and biological matter. *Phys. Rev. E* 87(4):042703.
110. MacKintosh F & Levine A (2008) Nonequilibrium mechanics and dynamics of motor-activated gels. *Phys. Rev. Lett.* 100:018104.
111. Wang S & Wolynes P (2012) Active contractility in actomyosin networks. *Proceedings of the National Academy of Sciences of the United States of America* 109(17):6446-6451.
112. Gadde S & Heald R (2004) Mechanisms and Molecules of the Mitotic Spindle. *Current Biology* 14(18):R797-R805.
113. Foster PJ, Furthauer S, Shelley MJ, & Needleman DJ (2015) Active contraction of microtubule networks. *eLife* 4.
114. Torisawa T, Taniguchi D, Ishihara S, & Oiwa K (Spontaneous Formation of a Globally Connected Contractile Network in a Microtubule-Motor System. *Biophysical Journal* 111(2):373-385.
115. Linsmeier I*, et al.* (2016) Disordered actomyosin networks are sufficient to produce cooperative and telescopic contractility. *Nature Communications* 7.
116. Schuppler M, Keber FC, Kroger M, & Bausch AR (2016) Boundaries steer the contraction of active gels. *Nature Communications* 7.
117. Spudich J & Watt S (1971) Regulation of Rabbit Skeletal Muscle Contraction. 1. Biochemical Studies of Interactions of Tropomyosin-Troponin Complex with Actin and Proteolytic Fragments of Myosin. *Journal of Biological Chemistry* 246(15):4866-&.
118. Margossian SS & Lowey S (1982) Preparation of Myosin and Its Subfragments from Rabbit Skeletal-Muscle. *Methods in Enzymology* 85:55-71.
119. Verkhovsky AB & Borisy GG (1993) Non-Sarcomeric Mode of Myosin-Ii Organization in the Fibroblast Lamellum. *Journal of Cell Biology* 123(3):637-652.

120. Craig S, Lancashire C, & Cooper J (1982) Preparation of Smooth-Muscle Alpha-Actinin. *Methods in Enzymology* 85:316-321.
121. Vignjevic D, Peloquin J, & Borisy GG (2006) In Vitro Assembly of Filopodia-Like Bundles. *Regulators and Effectors of Small GTPases: Rho Family*, (Academic Press), Vol Volume 406, pp 727-739.
122. Weirich K, Israelachvili J, & Fygenson D (2010) Bilayer Edges Catalyze Supported Lipid Bilayer Formation. *Biophysical Journal* 98(1):85-92.
123. Thevenaz P, Ruttimann UE, & Unser M (1998) A pyramid approach to subpixel registration based on intensity. *IEEE Trans Image Process* 7(1):27-41.
124. Schneider CA, Rasband WS, & Eliceiri KW (2012) NIH Image to ImageJ: 25 years of image analysis. *Nat Methods* 9(7):671-675.
125. Ishikawa R, Sakamoto T, Ando T, Higashi-Fujime S, & Kohama K (2003) Polarized actin bundles formed by human fascin-1: their sliding and disassembly on myosin II and myosin V in vitro. *Journal of Neurochemistry* 87(3):676-685.
126. Claessens M, Bathe M, Frey E, & Bausch AR (2006) Actin-binding proteins sensitively mediate F-actin bundle stiffness. *Nature Materials* 5(9):748-753.
127. Hartwig JH & Stossel TP (1979) Cytochalasin B and the structure of actin gels. *J Mol Biol* 134(3):539-553.
128. Hartwig JH & Stossel TP (1981) Structure of macrophage actin-binding protein molecules in solution and interacting with actin filaments. *J Mol Biol* 145(3):563-581.
129. Butler JP, Tolic-Norrelykke IM, Fabry B, & Fredberg JJ (2002) Traction fields, moments, and strain energy that cells exert on their surroundings. *Am J Physiol Cell Physiol* 282(3):C595-605.
130. Murrell M & Gardel ML (2014) Actomyosin sliding is attenuated in contractile biomimetic cortices. *Molecular Biology of the Cell* 25(12):1845-1853.
131. Freedman S, Banerjee S, Hocky GM, & Dinner AR (2016) A versatile framework for simulating the dynamic mechanical structure of cytoskeletal networks. (arXiv:1609.05202).
132. Nedelec FJ, Surrey T, Maggs AC, & Leibler S (1997) Self-organization of microtubules and motors. *Nature* 389(6648):305-308.
133. Urrutia R, McNiven MA, Albanesi JP, Murphy DB, & Kachar B (1991) Purified Kinesin Promotes Vesicle Motility and Induces Active Sliding between Microtubules Invitro. *Proceedings of the National Academy of Sciences of the United States of America* 88(15):6701-6705.
134. Koehler S, Schaller V, & Bausch AR (2011) Structure formation in active networks. *Nature Materials* 10(6):462-468.
135. Soares e Silva M*, et al.* (2011) Active multistage coarsening of actin networks driven by myosin motors. *Proceedings of the National Academy of Sciences of the United States of America* 108(23):9408-9413.
136. Backouche F, Haviv L, Groswasser D, & Bernheim-Groswasser A (2006) Active gels: dynamics of patterning and self-organization. *Phys Biol* 3(4):264-273.
137. Jülicher F, Kruse K, Prost J, & Joanny JF (2007) Active behavior of the Cytoskeleton. *Physics Reports* 449(1–3):3-28.
138. Zidovska A, Weitz DA, & Mitchison TJ (2013) Micron-scale coherence in interphase chromatin dynamics. *Proc Natl Acad Sci U S A* 110(39):15555-15560.

139. Yan J, Sharo AG, Stone HA, Wingreen NS, & Bassler BL (2016) Vibrio cholerae biofilm growth program and architecture revealed by single-cell live imaging. *Proceedings of the National Academy of Sciences* 113(36):E5337-E5343.
140. Asally M*, et al.* (2012) Localized cell death focuses mechanical forces during 3D patterning in a biofilm. *Proceedings of the National Academy of Sciences* 109(46):18891-18896.
141. Harris AK, Stopak D, & Wild P (1981) Fibroblast traction as a mechanism for collagen morphogenesis. *Nature* 290(5803):249-251.
142. Vader D, Kabla A, Weitz D, & Mahadevan L (2009) Strain-Induced Alignment in Collagen Gels. *PLOS ONE* 4(6):e5902.
143. Cetera M*, et al.* (2014) Epithelial rotation promotes the global alignment of contractile actin bundles during Drosophila egg chamber elongation. *Nat Commun* 5:5511.
144. Zemel A, Rehfeldt F, Brown AE, Discher DE, & Safran SA (2010) Optimal matrix rigidity for stress fiber polarization in stem cells. *Nat Phys* 6(6):468-473.
145. Oakes PW, Banerjee S, Marchetti MC, & Gardel ML (2014) Geometry regulates traction stresses in adherent cells. *Biophys J* 107(4):825-833.
146. Thoresen T, Lenz M, & Gardel M (2013) Thick Filament Length and Isoform Composition Determine Self-Organized Contractile Units in Actomyosin Bundles. *Biophysical Journal* 104(3):655-665.
147. Mandal K, Wang I, Vitiello E, Orellana LA, & Balland M (2014) Cell dipole behaviour revealed by ECM sub-cellular geometry. *Nat Commun* 5:5749.
148. Tanimoto H & Sano M (2014) A Simple Force-Motion Relation for Migrating Cells Revealed by Multipole Analysis of Traction Stress. *Biophysical Journal* 106(1):16-25.
149. Tanimoto H & Sano M (2012) Dynamics of traction stress field during cell division. *Phys Rev Lett* 109(24):248110.
150. Tambe DT*, et al.* (2011) Collective cell guidance by cooperative intercellular forces. *Nat Mater* 10(6):469-475.